

ELECTRONIC SUPPLEMENTARY INFORMATION

**Alkyl melibioside and alkyl cellobioside surfactants:
Effect of sugar headgroup and alkyl chain length on performance**

Laurel L. Kegel, Lajos Z. Szabó, Robin Polt, Jeanne E. Pemberton^{§†}

Department of Chemistry and Biochemistry
University of Arizona
1306 E. University Boulevard
Tucson, Arizona 85721, United States

[§] Corresponding author: pembertn@email.arizona.edu

[†] Conflict of Interest: One of the authors (JEP) has equity ownership in an entity that is developing products related to the research being reported. The terms of this arrangement have been reviewed and approved by the University of Arizona in accordance with its policy on objectivity in research.

Characterization Data for Glycolipids

Table S1. Results of InBr₃ Promoted Glycosidations

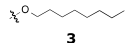
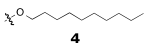
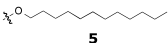
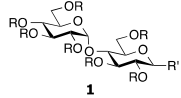
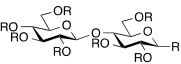
<p>β-Peracetyl Donors</p> <p>R = Ac, R' = β-OAc</p>	Acceptors											
	R' = 				R' = 				R' = 			
	R=Ac		R=H		R=Ac		R=H		R=Ac		R=H	
	#	#	Calc. M 454.2 Found (M+Na) ⁺	Combined yield %	#	#	Calc. M 482.3 Found (M+Na) ⁺	Combined yield %	#	#	Calc. M 510.3 Found (M+Na) ⁺	Combined yield %
 <p>1</p>	6a	6	477.2	88	7a	7	505.3	66	8a	8	533.2	76
	 <p>2</p>	9a	9	477.3	85	10a	10	505.3	87	11a	11	533.3

Table S2. ¹H NMR data of Peracetyl SurfactantsChemical shifts δ (ppm), J (Hz) and proton numbers

	H1 and H1'		COCH ₃				CH ₂ -s				CH ₃	
6a,α	5.02	d, 3.6, 1H	4.86	d, 3.7, 1H	1.99, 1.97, 1.91, 1.90, 1.90, 1.86, 1.83	7s, 21H	1.50-1.43	m, 2H	1.26-1.11	m, 10H	0.74	tr, 3H
6a,β	5.10	d, 3.7, 1H	4.42	d, 8.0, 1H	1.99, 1.97, 1.91, 1.90, 1.90, 1.86, 1.83	7s, 21H	1.57-1.44	m, 2H	1.30-1.17	m, 10H	0.82	tr, 3H
7a,α	5.14	d, 3.6, 1H	4.97	d, 3.7, 1H	2.10, 2.08, 2.03, 2.02, 2.01, 1.98, 1.95	7s, 21H	1.60-1.53	m, 2H	1.33-1.21	m, 14H	0.85	tr, 3H
7a,β	5.10	d, 3.7, 1H	4.43	d, 8.1, 1H	2.08, 2.07, 2.00, 1.99, 1.98, 1.95, 1.94	7s, 21H	1.54-1.46	m, 2H	1.26-1.18	m, 14H	0.83	tr, 3H
8a,α	5.11	d, 3.6, 1H	4.95	d, 3.6, 1H	2.07, 2.05, 1.99, 1.99, 1.98, 1.94, 1.91	7s, 21H	1.57-1.50	m, 2H	1.31-1.18	m, 18H	0.82	tr, 3H
8a,β	5.10	d, 3.7, 1H	4.42	d, 8.0, 1H	2.07, 2.06, 1.98, 1.98, 1.97, 1.94, 1.92	7s, 21H	1.51-1.45	m, 2H	1.25-1.17	m, 18H	0.82	tr, 3H
9a,α	4.84	d, 3.7, 1H	4.40	d, 8.0, 1H	1.99, 1.95, 1.91, 1.90, 1.89, 1.88, 1.85	7s, 21H	1.49-1.42	m, 2H	1.21-1.12	m, 10H	0.75	tr, 3H
9a,β	4.40	d, 8.0, 1H	4.32	d, 8.0, 1H	1.97, 1.94, 1.89, 1.88, 1.87, 1.86, 1.83	7s, 21H	1.47-1.36	m, 2H	1.20-1.09	m, 10H	0.73	tr, 3H
10a,α	4.92	d, 3.8, 1H	4.46	d, 7.9, 1H	2.08, 2.04, 2.00, 1.99, 1.97, 1.96, 1.93	7s, 21H	1.56-1.50	m, 2H	1.27-1.19	m, 14H	0.83	tr, 3H
10a,β	4.47	d, 7.9, 1H	4.40	d, 7.9, 1H	2.08, 2.04, 1.99, 1.99, 1.98, 1.97, 1.94	7s, 21H	1.56-1.49	m, 2H	1.27-1.18	m, 14H	0.84	tr, 3H
11a,α	4.91	d, 3.6, 1H	4.46	d, 8.0, 1H	2.08, 2.04, 2.00, 1.99, 1.98, 1.96, 1.94	7s, 21H	1.58-1.50	m, 2H	1.30-1.19	m, 18H	0.83	tr, 3H
11a,β	4.47	d, 7.7, 1H	4.34	d, 8.1, 1H	2.05, 2.01, 1.96, 1.95, 1.95, 1.94, 1.91	7s, 21H	1.54-1.45	m, 2H	1.24-1.16	m, 18H	0.81	tr, 3H

Table S3. ¹H NMR data of Glycolipid Surfactants

	Chemical shifts δ (ppm), J (Hz) and proton numbers																									
	H1 and H1'		H2, H3, H4, H5, H6, H2', H3', H4', H5' and H6'														CH ₂ -s		CH ₃							
6, α	4.89	d, 3.0, 1H	4.79	d, 3.8, 1H	3.97-3.88	m, 3H	3.80-3.69	m, 7H	3.65	tr, 1H	3.48-3.40	m, 3H							1.67-1.59	m, 2H	1.44-1.29	m, 10H	0.90	tr, 3H		
6, β	4.88	d, 2.0, 1H	4.29	d, 7.9, 1H	3.92-3.80	m, 3H	3.77-3.68	m, 5H	3.58-3.52	m, 1H	3.50-3.35	m, 4H	3.21	tr, 1H						1.66-1.59	m, 2H	1.40-1.29	m, 10H	0.90	tr, 3H	
a, α	4.88	d, 3.0, 1H	4.79	d, 3.6, 1H	3.97	dd, 1H	3.92-3.89	m, 2H	3.77-3.62	m, 8H	3.47-3.37	m, 3H								1.68-1.60	m, 2H	1.42-1.26	m, 14H	0.90	tr, 3H	
7, β	4.80	n/d	4.31	d, 7.9, 1H	4.01	dd, 1H	3.93-3.85	m, 3H	3.78-3.77	m, 2H	3.73-3.69	m, 3H	3.60-3.55	m, 1H	3.50	ddd, 1H	3.46-3.36	m, 2H	3.22	tr, 1H	1.69-1.62	m, 2H	1.43-1.30	m, 14H	0.93	tr, 3H
8, α	4.91	d, 3.4, 1H	4.80	d, 3.8, 1H	3.99	dd, 1H	3.94	m, 1H	3.90	tr, 1H	3.79	tr, 2H	3.76-3.63	m, 6H	3.48-3.42	m, 3H				1.67-1.60	m, 2H	1.41-1.29	m, 18H	0.90	tr, 3H	
8, β	4.80	n/d	4.30	d, 7.9, 1H	4.00	dd, 1H	3.93-3.83	m, 3H	3.79-3.77	m, 2H	3.72-3.67	m, 3H	3.70-3.52	m, 1H	3.50-3.40	m, 2H	3.38	tr, 1H	3.21	tr, 1H	1.68-1.60	m, 2H	1.42-1.27	m, 18H	0.90	tr, 3H
9, α	4.77	d, 3.8, 1H	4.40	d, 7.6, 1H	3.91-3.87	m, 2H	3.82-3.65	m, 4H	3.58-3.51	m, 2H	3.49-3.42	m, 2H	3.41-3.30	m, 3H	3.24	dd, 1H				1.67-1.59	m, 2H	1.42-1.29	m, 10H	0.91	tr, 3H	
9, β	4.44	d, 8.1, 1H	4.32	d, 7.9, 1H	3.92-3.80	m, 4H	3.65-3.57	m, 2H	3.54-3.48	m, 2H	3.45-3.34	m, 3H	3.30-3.24	m, 2H	3.20	tr, 1H				1.71-1.64	m, 2H	1.47-1.38	m, 10H	0.91	tr, 3H	
10, α	4.77	d, 3.8, 1H	4.10	d, 7.8, 1H	3.92-3.87	m, 2H	3.80	dd, 1H	3.72-3.65	m, 4H	3.55	dd, 1H	3.49-3.44	m, 2H	3.42-3.40	m, 3H	3.24	dd, 1H		1.67-1.59	m, 2H	1.41-1.27	m, 14H	0.90	tr, 3H	
10, β	4.42	d, 7.8, 1H	4.28	d, 7.8, 1H	3.91-3.85	m, 4H	3.66	dd, 1H	3.59-3.49	m, 3H	3.41-3.83	m, 4H	3.27-3.21	m, 2H						1.66-1.59	m, 2H	1.40-1.26	m, 14H	0.90	tr, 3H	
11, α	4.60	d, 3.6, 1H	4.22	d, 7.9, 1H	3.76-3.14	m, 10H	3.16	tr, 2H	3.06	tr, 1H	2.99	tr, 1H								1.53-1.48	m, 2H	1.29-1.19	m, 18H	0.85	tr, 3H	
11, β	4.24	d, 7.9, 1H	4.15	d, 7.9, 1H	3.76-2.96	m, 14H														1.52-1.47	m, 2H	1.30-1.19	m, 18H	0.85	tr, 3H	

NMR Spectra of Alkyl-O- Acetyl-Melibiosides ($^1\text{H-NMR}$, Expanded $^1\text{H-NMR}$, $^{13}\text{C-NMR}$, and Expanded $^{13}\text{C-NMR}$).

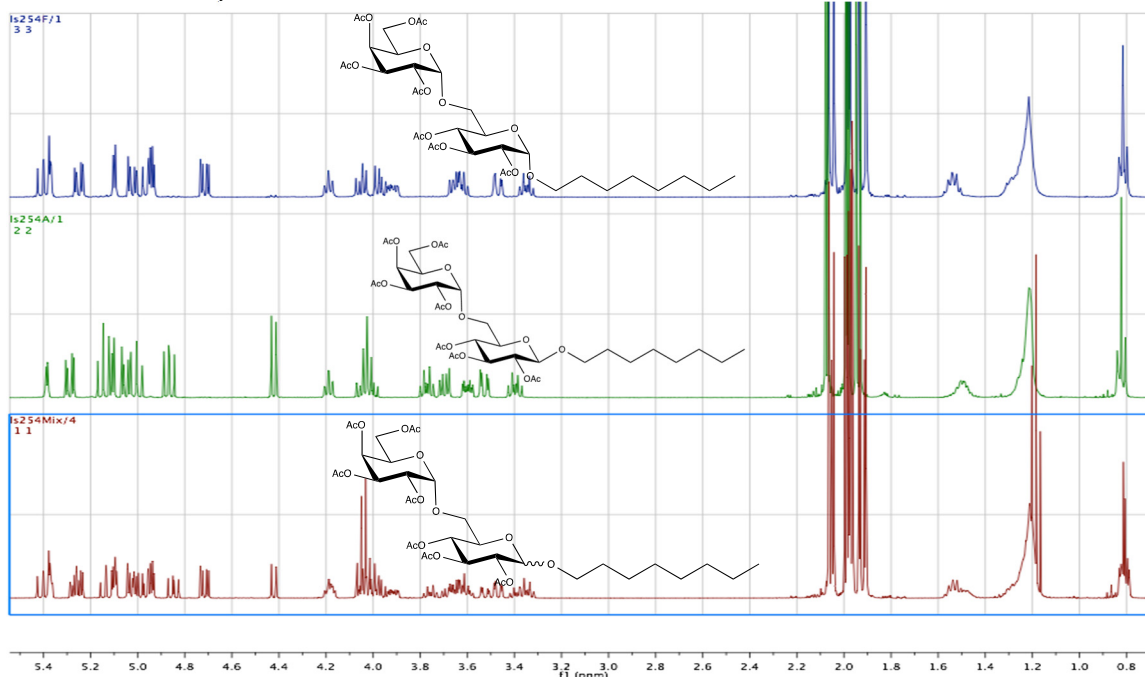


Figure S1a. $^1\text{H-NMR}$ Spectra of Octyl-O-acetyl melibioside (**6a**)

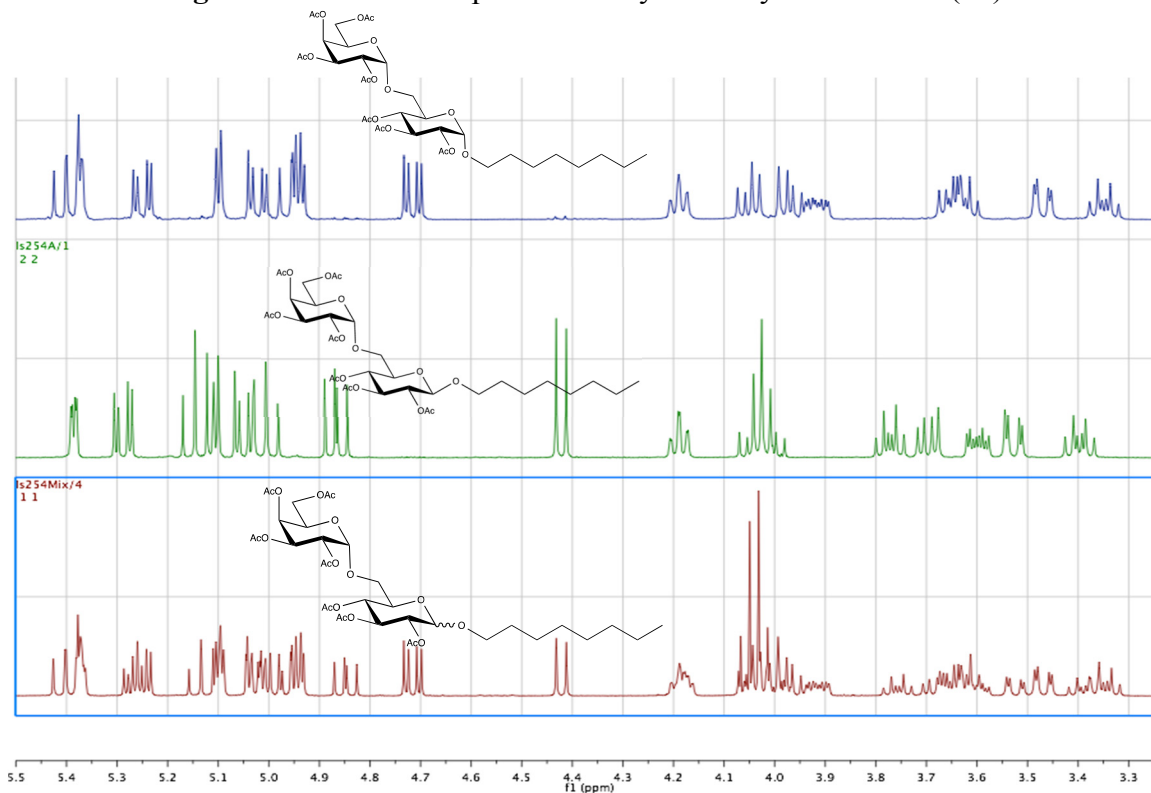


Figure S1b. Expanded $^1\text{H-NMR}$ Spectra of Octyl-O-acetyl melibioside (**6a**)

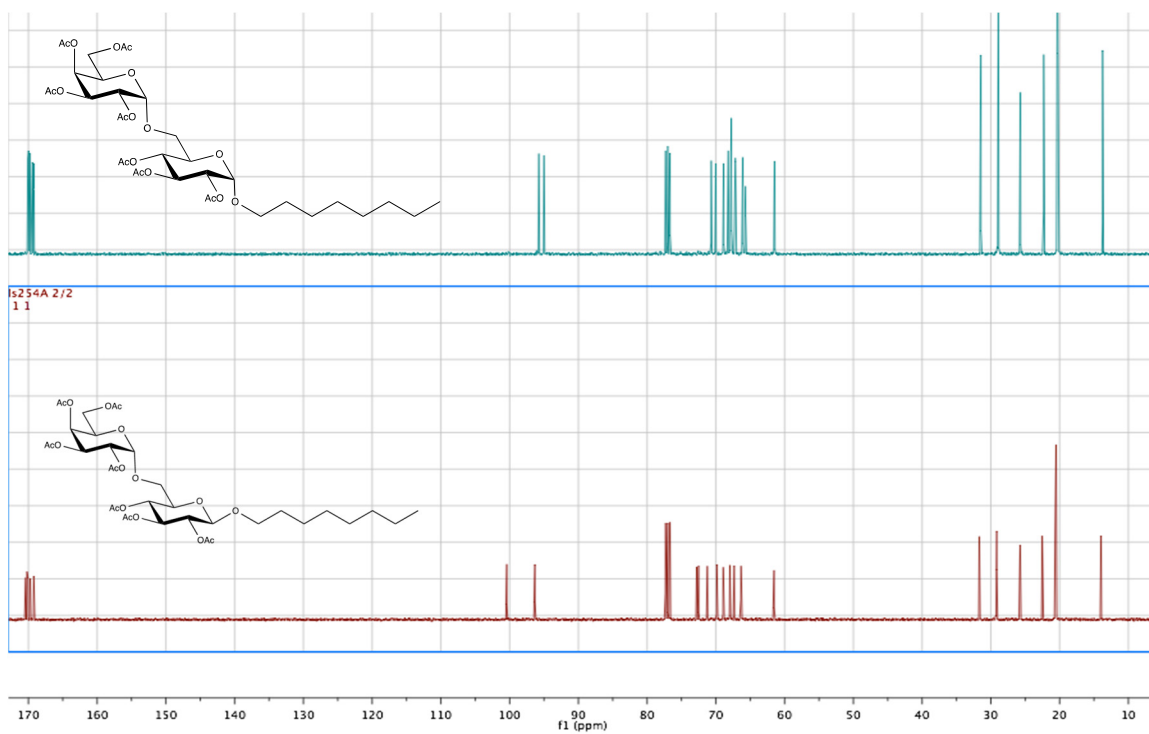


Figure S1c. ^{13}C -NMR Spectra of Octyl-O-acetyl melibioside (6a)

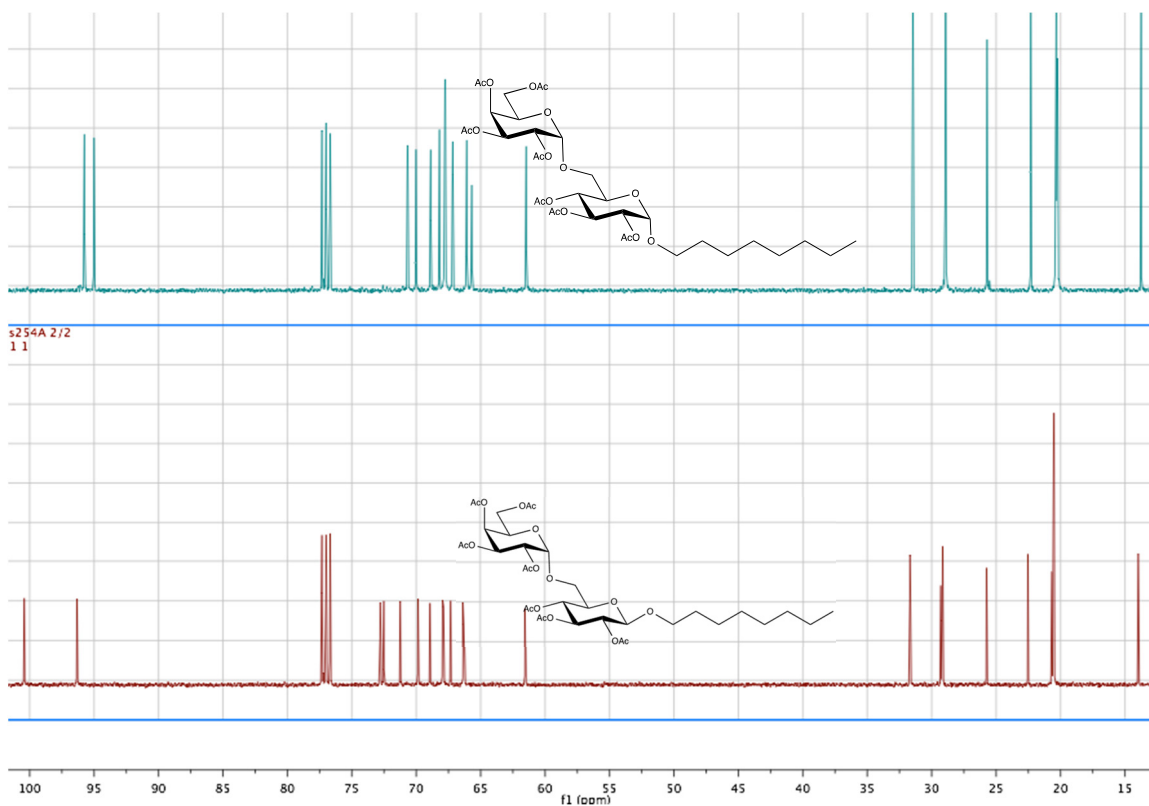


Figure S1d. Expanded ^{13}C -NMR Spectra of Octyl-O-acetyl melibioside (6a)

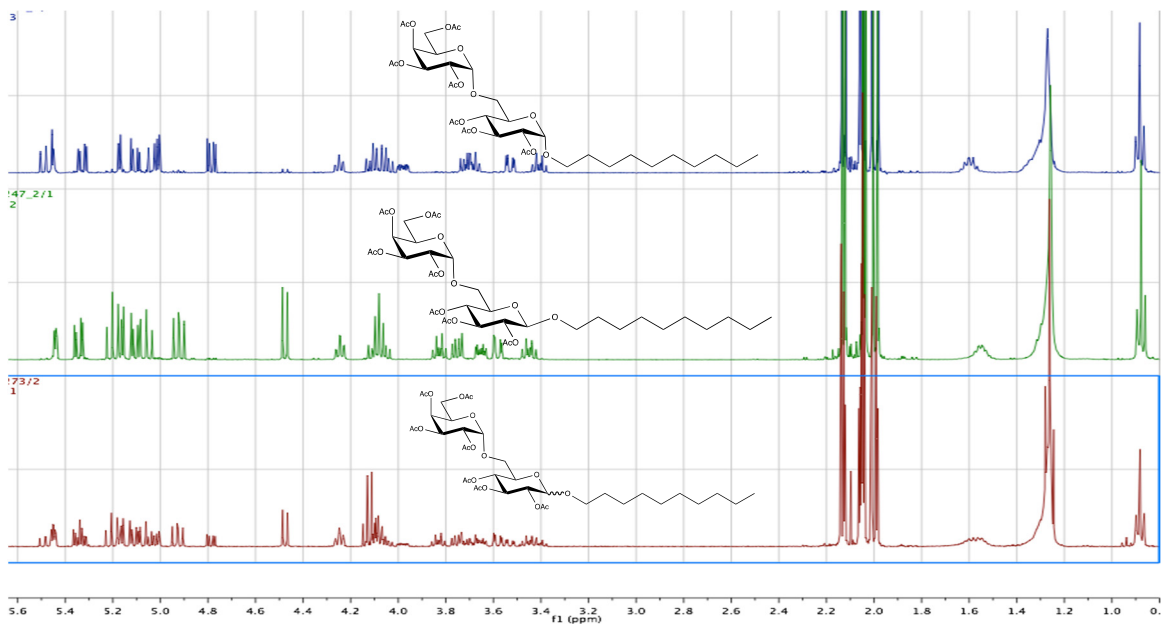


Figure S2a. $^1\text{H-NMR}$ Spectra of Decyl-O-acetyl melibioside (7a)

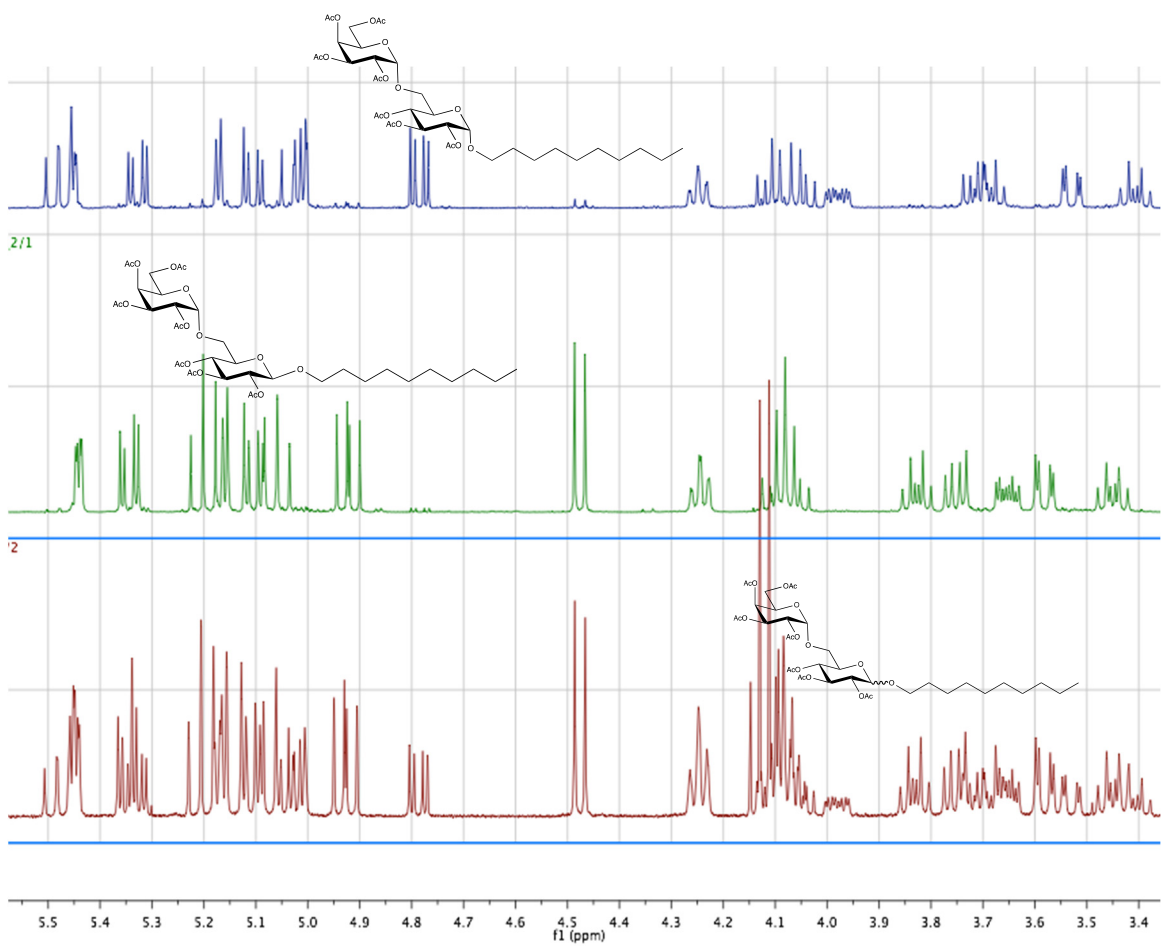


Figure S2b. Expanded $^1\text{H-NMR}$ Spectra of Decyl-O-acetyl melibioside

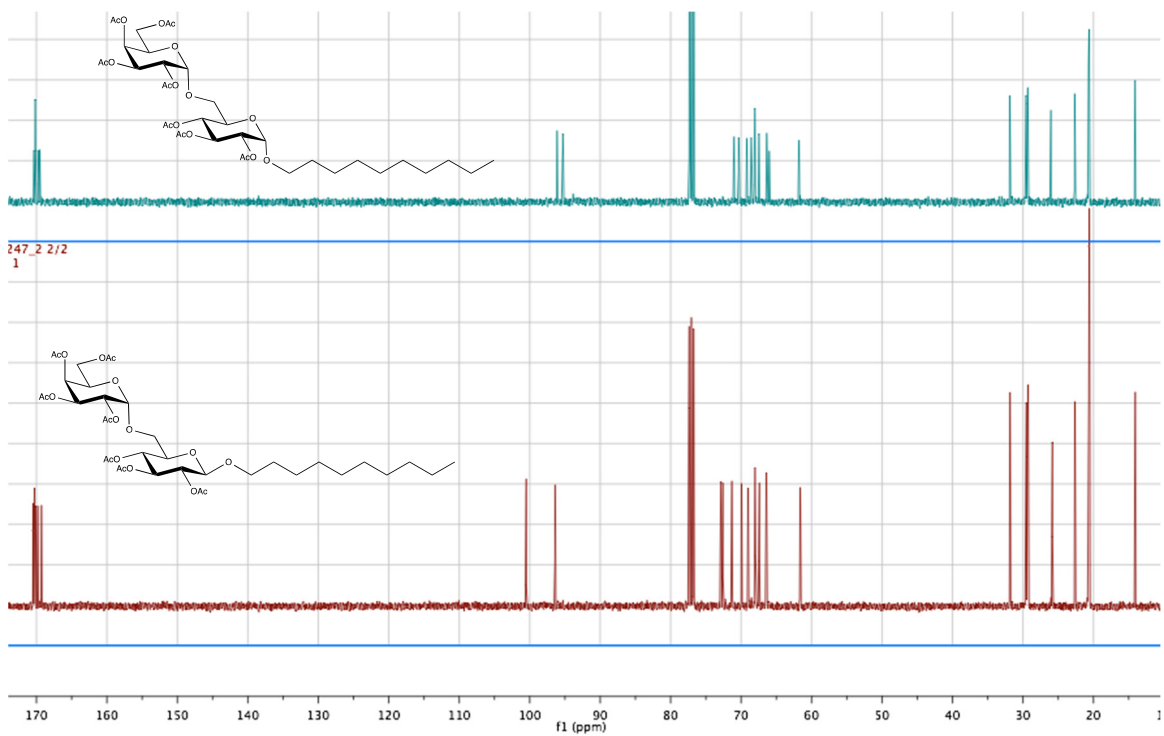


Figure S2c. ^{13}C -NMR Spectra of Decyl-O-acetyl melibioside (7a)

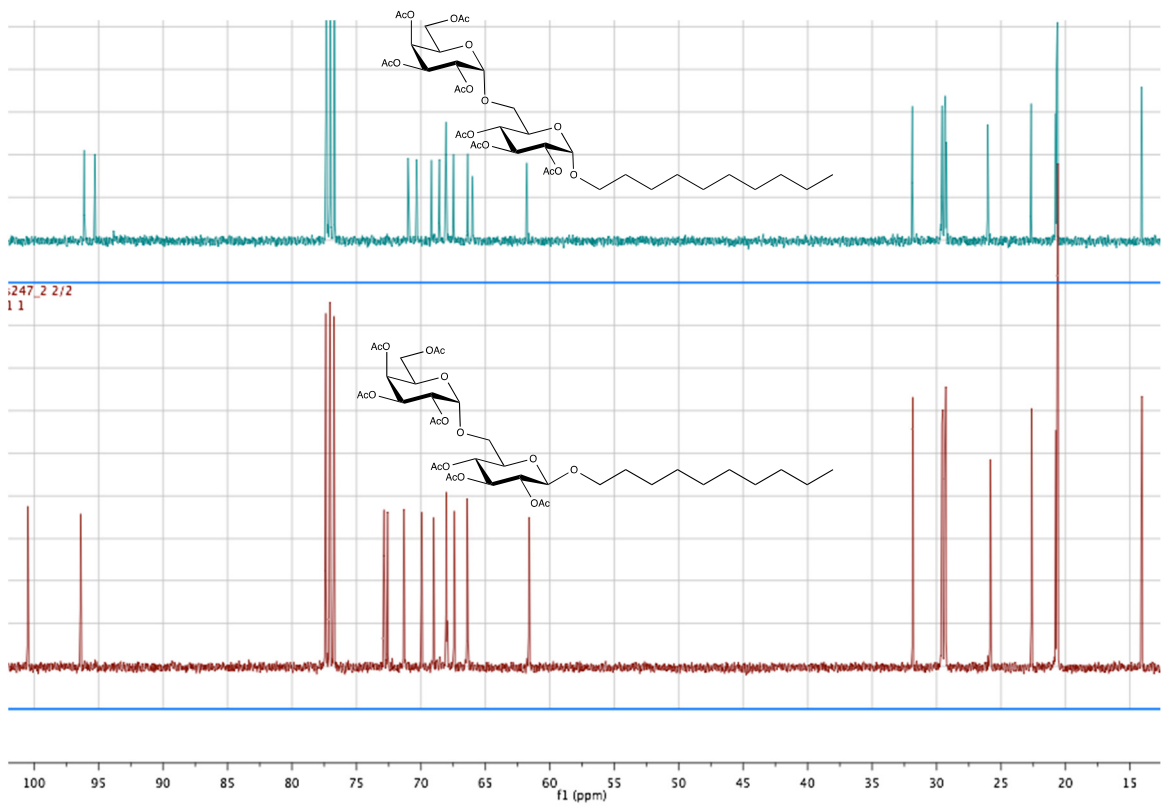


Figure S2d. Expanded ^{13}C -NMR Spectra of Decyl-O-acetyl melibioside (7a)

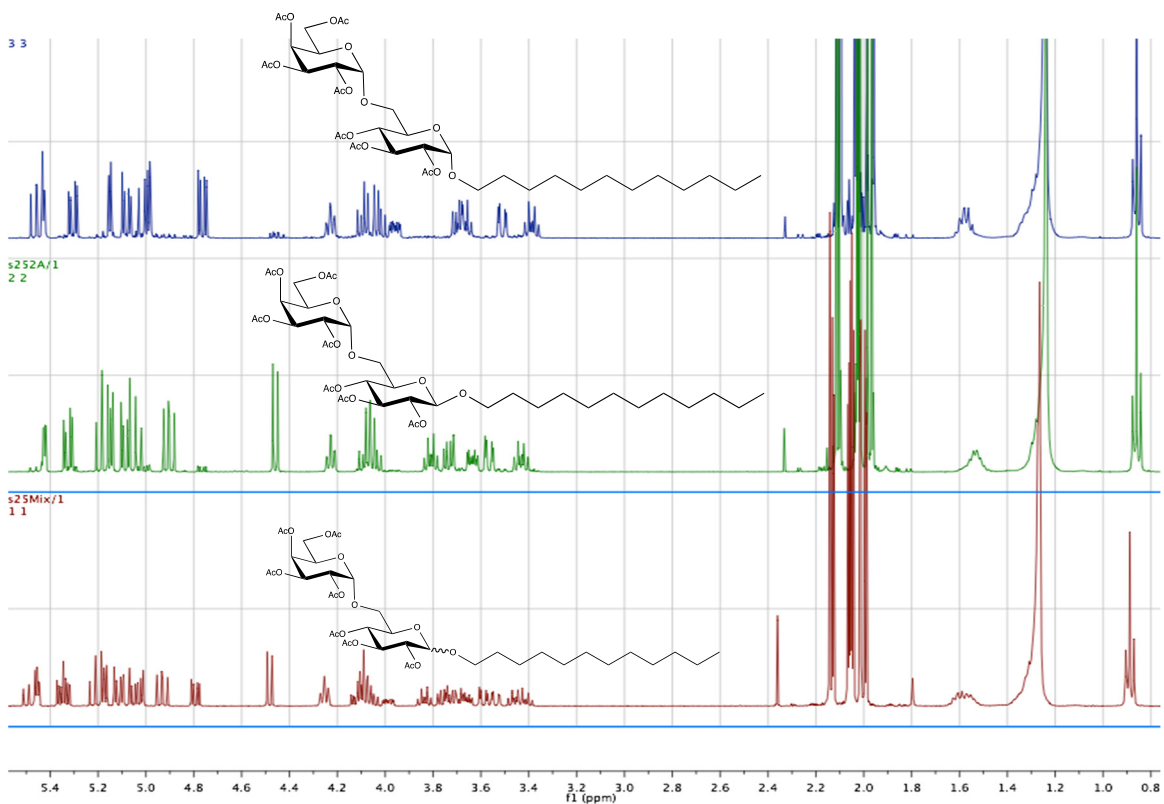


Figure S3a. $^1\text{H-NMR}$ Spectra of Dodecyl-O-acetyl melibioside (**8a**)

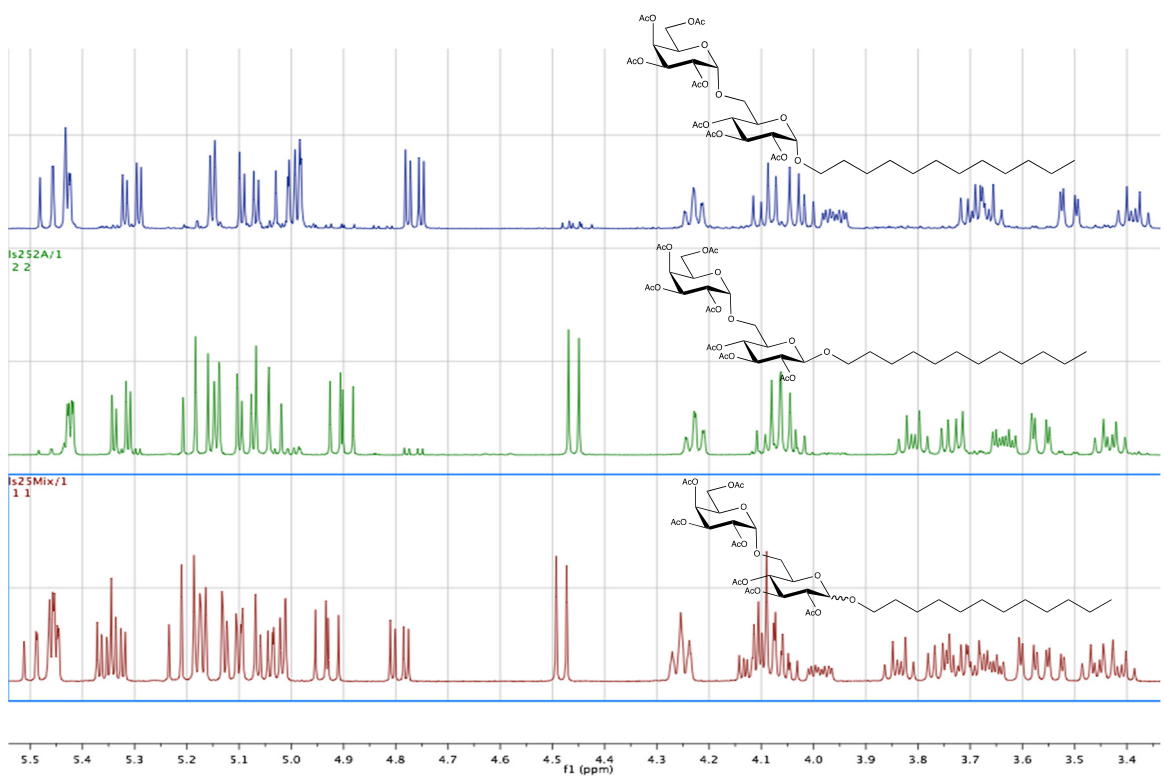


Figure S3b. Expanded $^1\text{H-NMR}$ Spectra of Dodecyl-O-acetyl melibioside (**8a**)

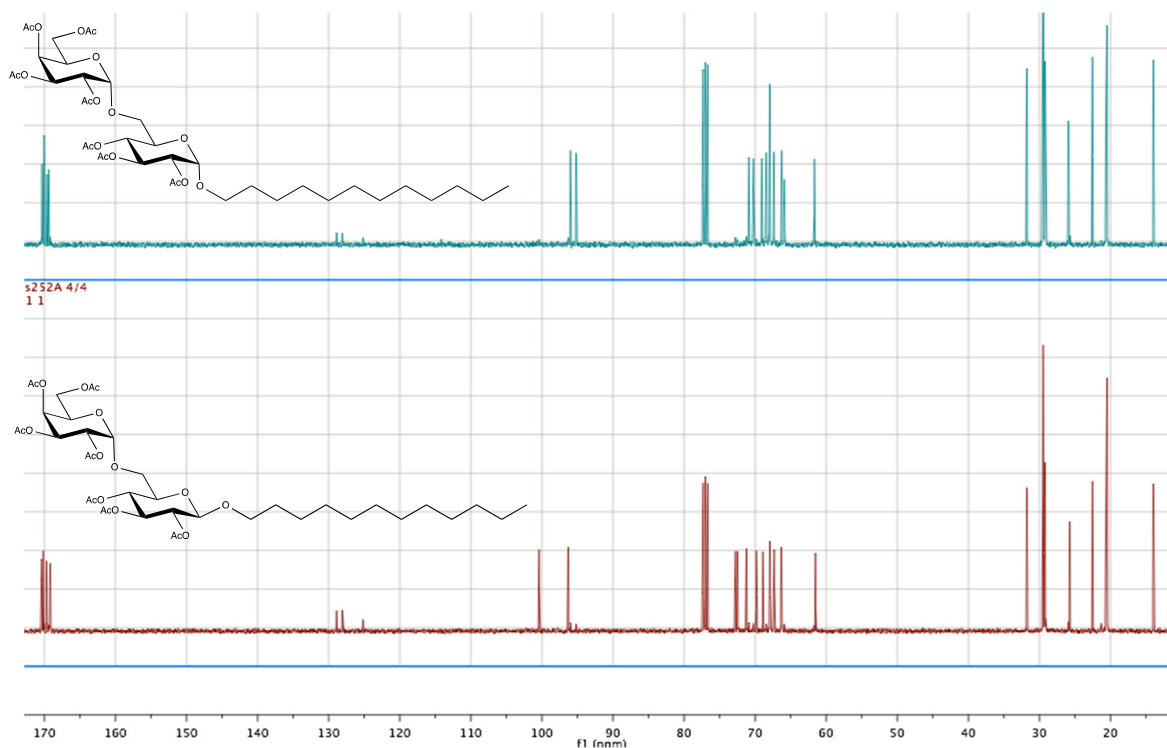


Figure S3c. ^{13}C -NMR Spectra of Dodecyl-O-acetyl melibioside (8a)

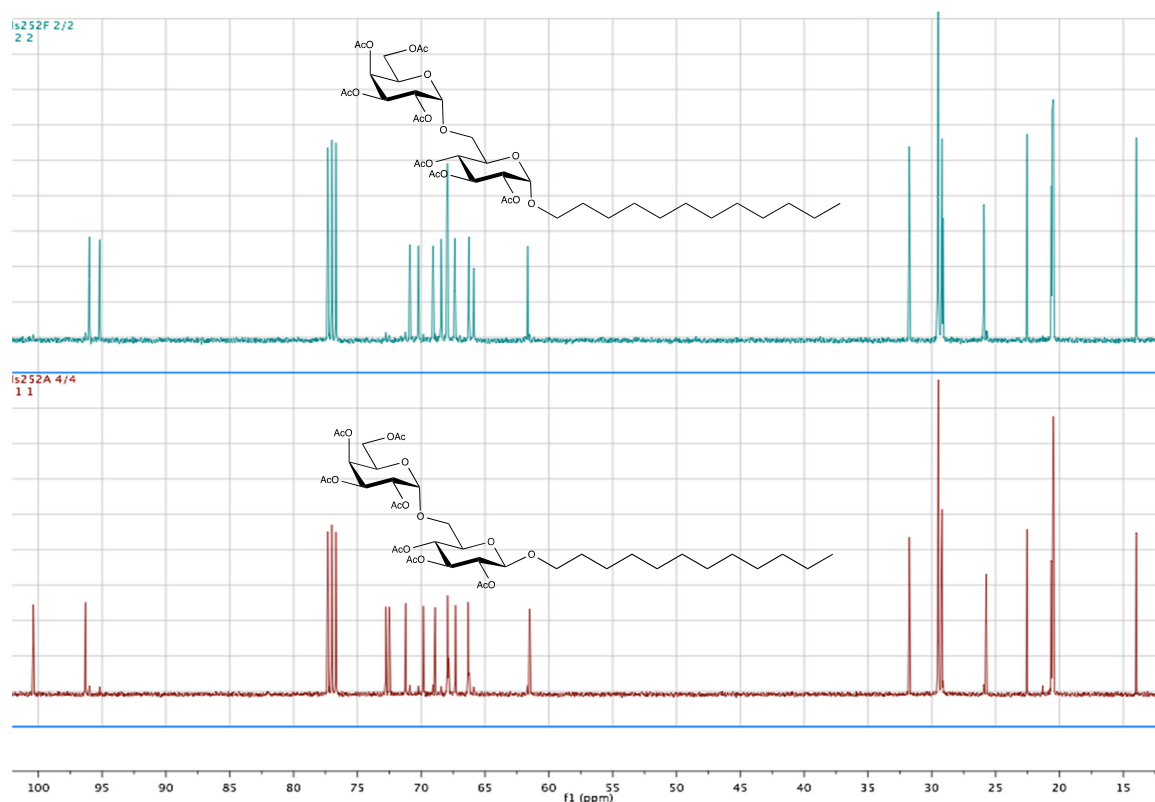
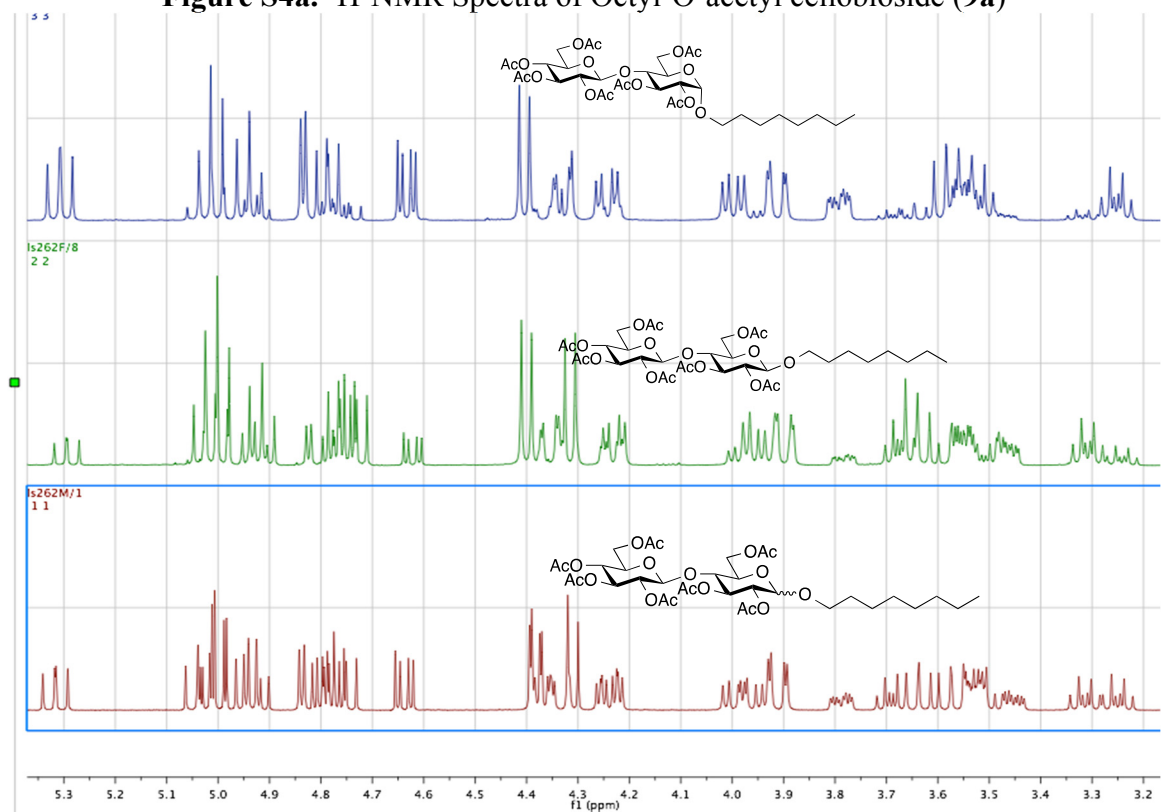
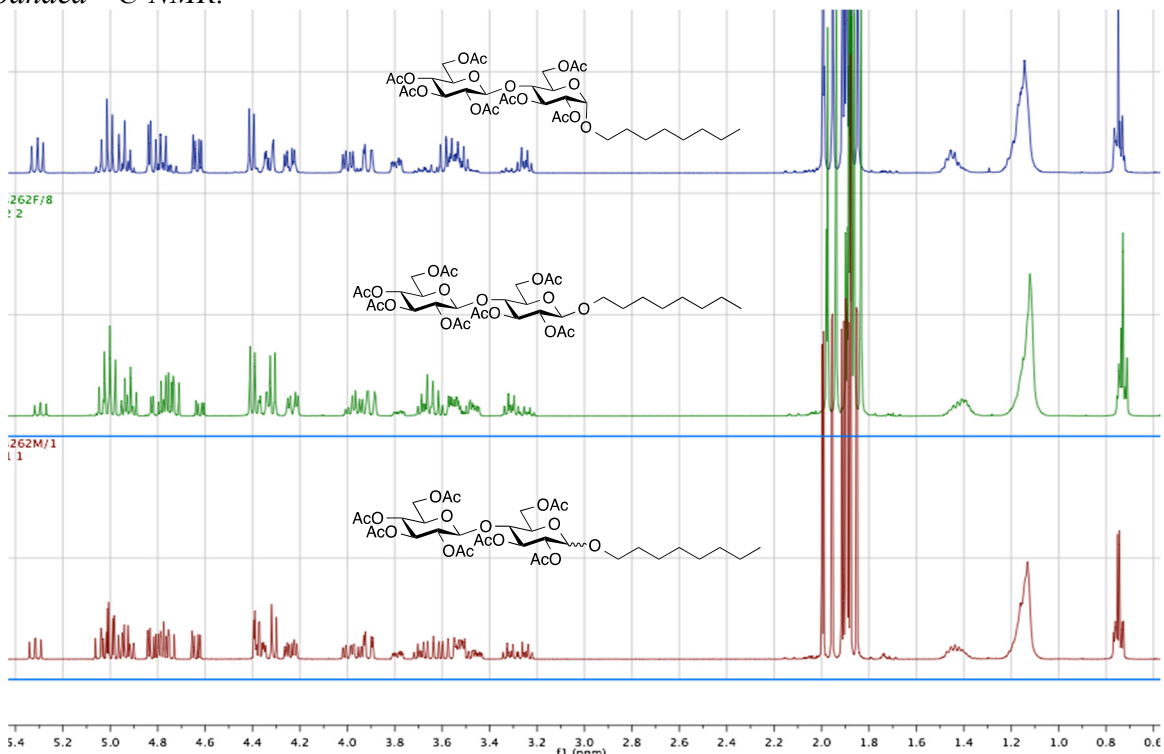


Figure S3d. Expanded ^1H -NMR Spectra of Dodecyl-O-acetyl melibioside (8a)

NMR Spectra of Alkyl-O- Acetyl-Cellobiosides (¹H-NMR, Expanded ¹H-NMR, ¹³C-NMR, and Expanded ¹³C-NMR.



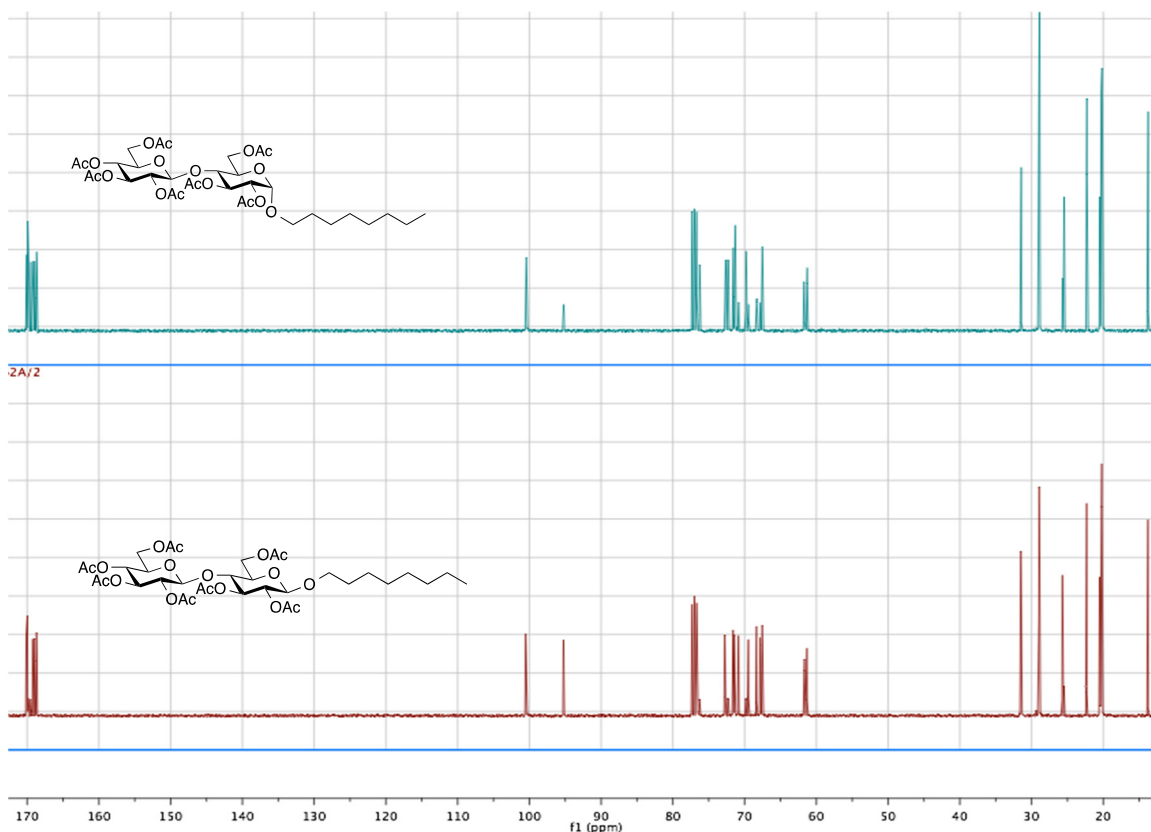


Figure S4c. ^{13}C -NMR Spectra of Octyl-O-acetyl cellobioside (**9a**)

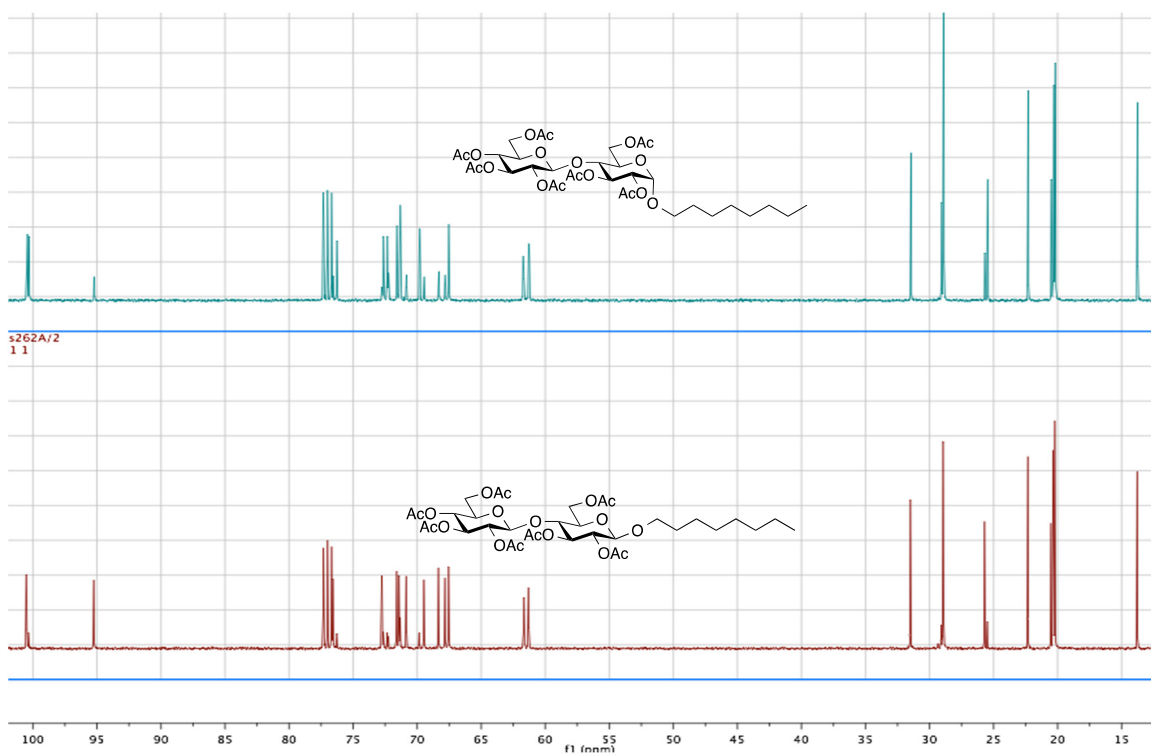


Figure S4d. Expanded ^{13}C -NMR Spectra of Octyl-O-acetyl cellobioside (**9a**)

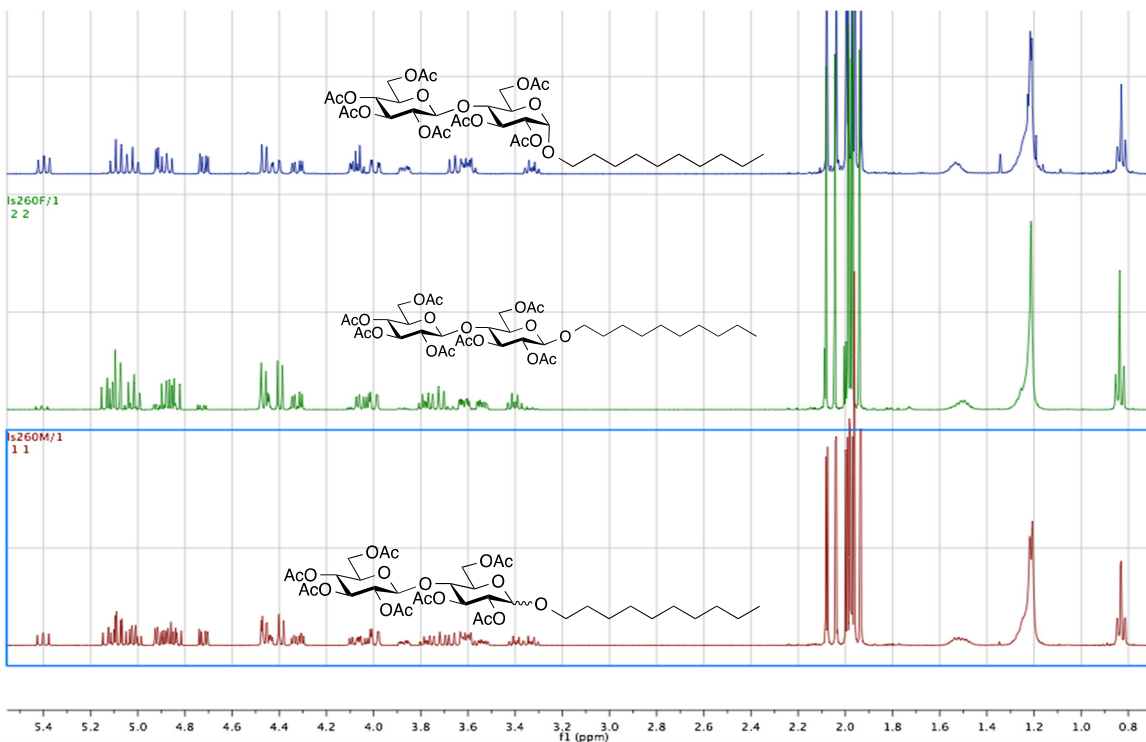


Figure S5a. $^1\text{H-NMR}$ Spectra of Decyl-O-acetyl cellobioside (10a)

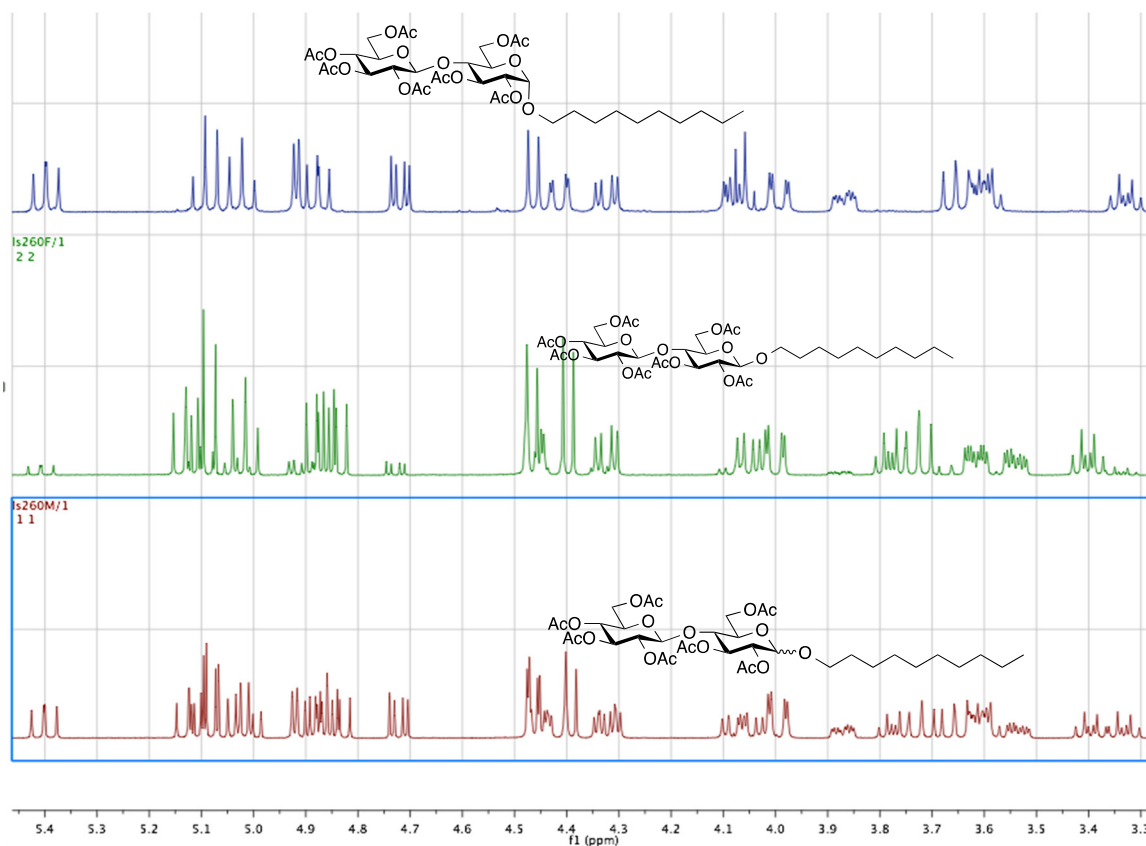


Figure S5b. Expanded $^1\text{H-NMR}$ Spectra of Decyl-O-acetyl cellobioside (10a)

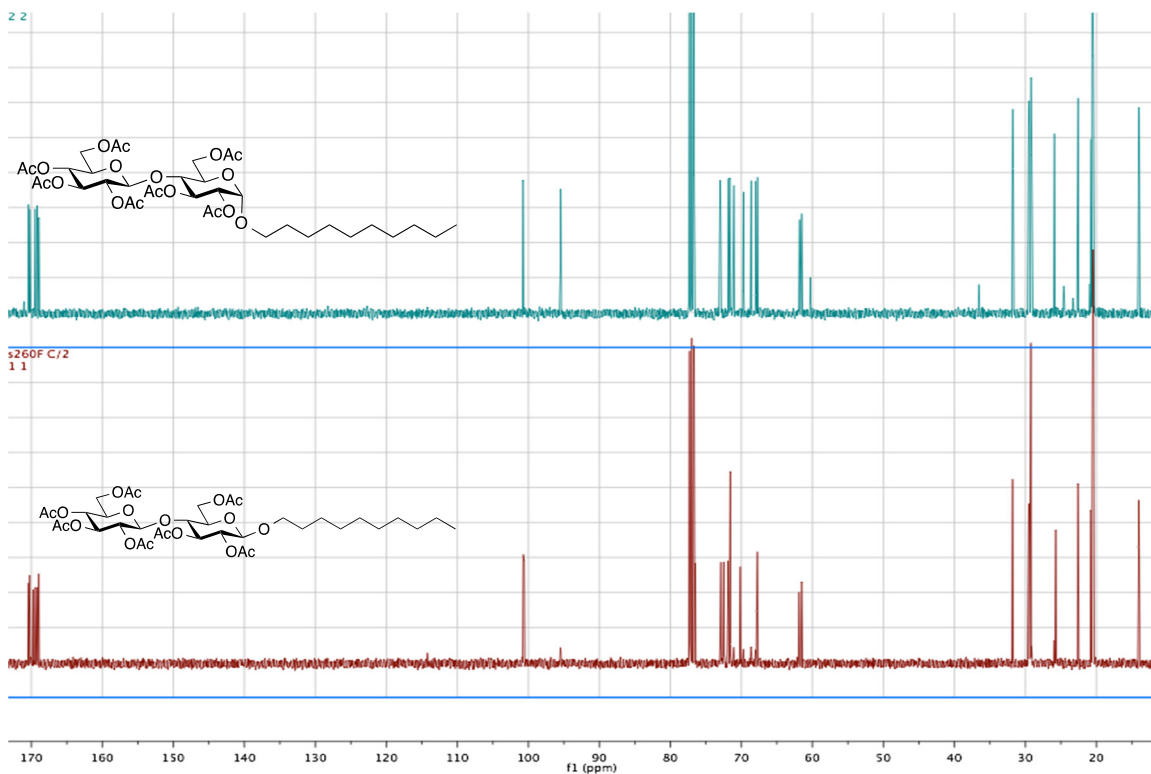


Figure S5c. ^{13}C -NMR Spectra of Decyl-O-acetyl cellobioside (10a)

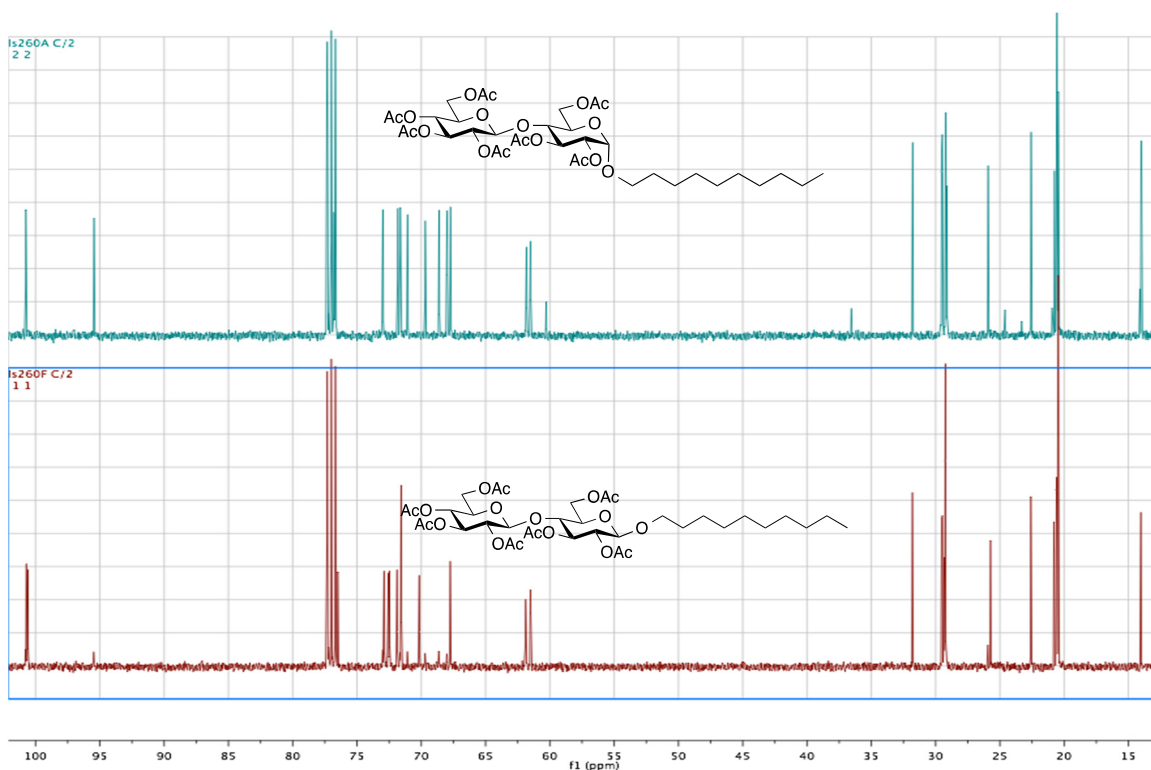


Figure S5d. Expanded ^{13}C -NMR Spectra of Decyl-O-acetyl cellobioside (10a)

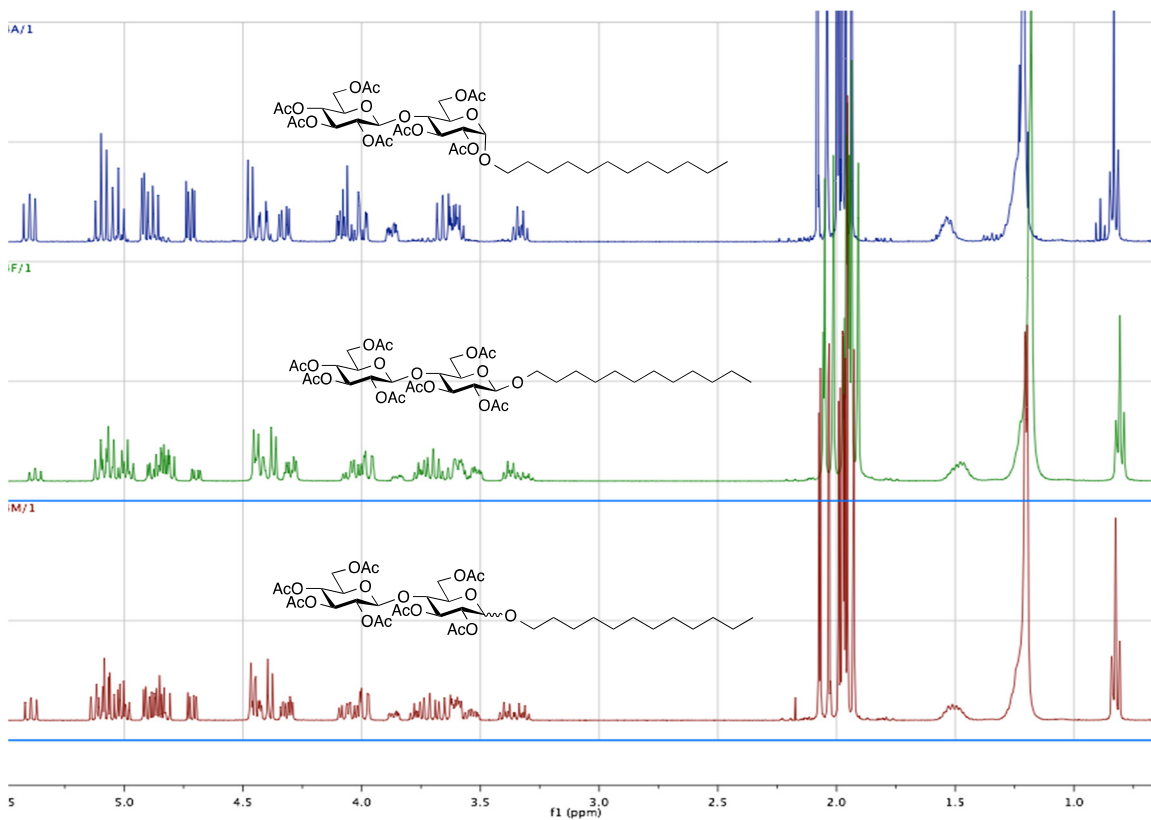


Figure S6a. $^1\text{H-NMR}$ Spectra of Dodecyl-O-acetyl cellobioside (11a)

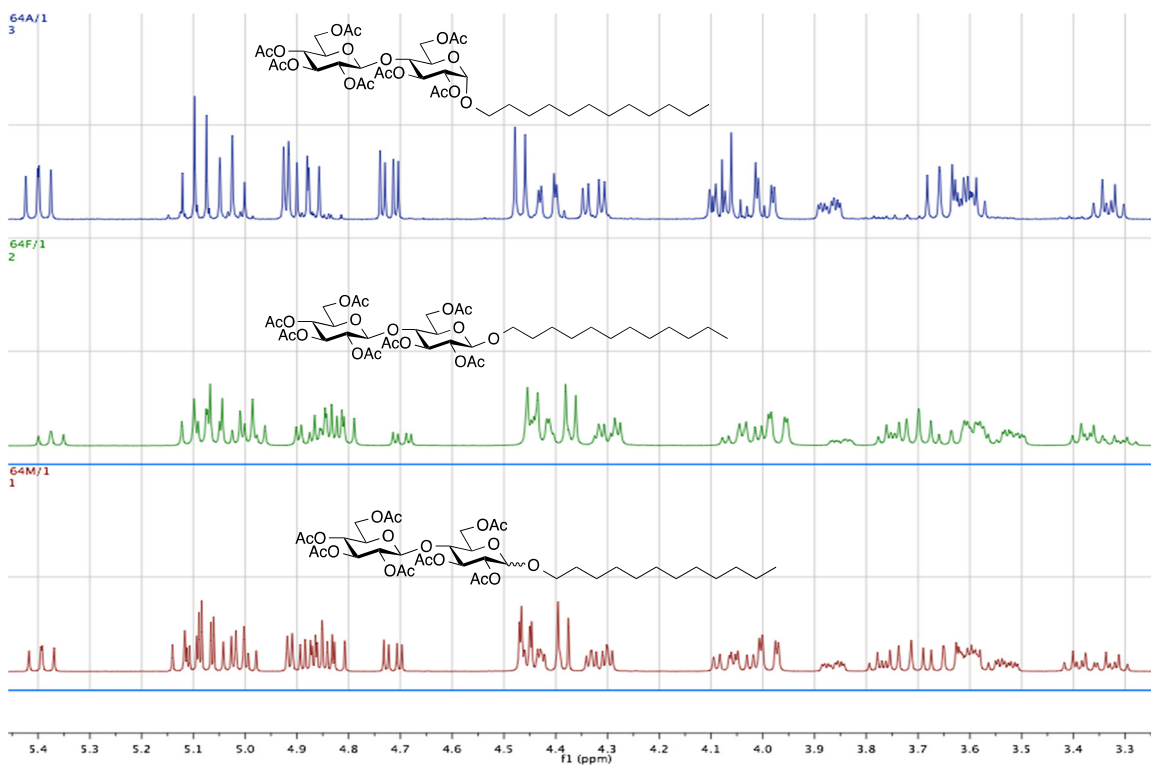


Figure S6b. Expanded $^1\text{H-NMR}$ Spectra of Dodecyl-O-acetyl cellobioside (11a)

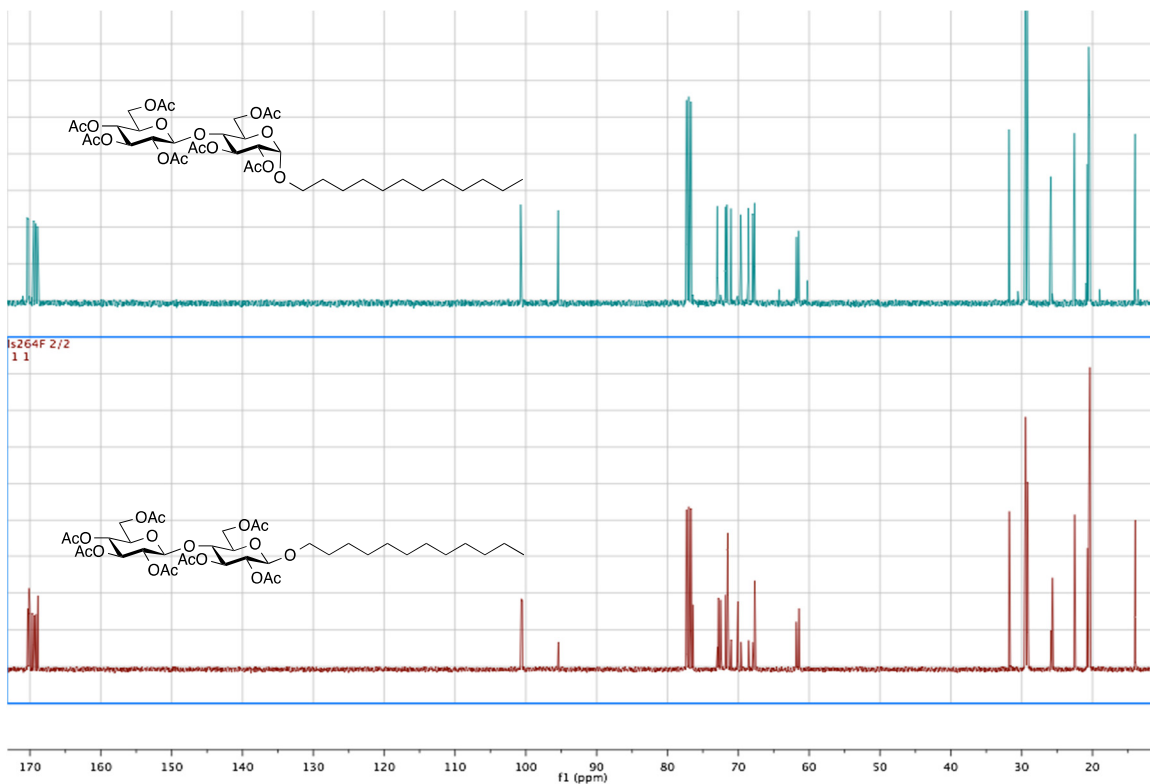


Figure S6c. ^{13}C -NMR Spectra of Dodecyl-O-acetyl cellobioside (11a)

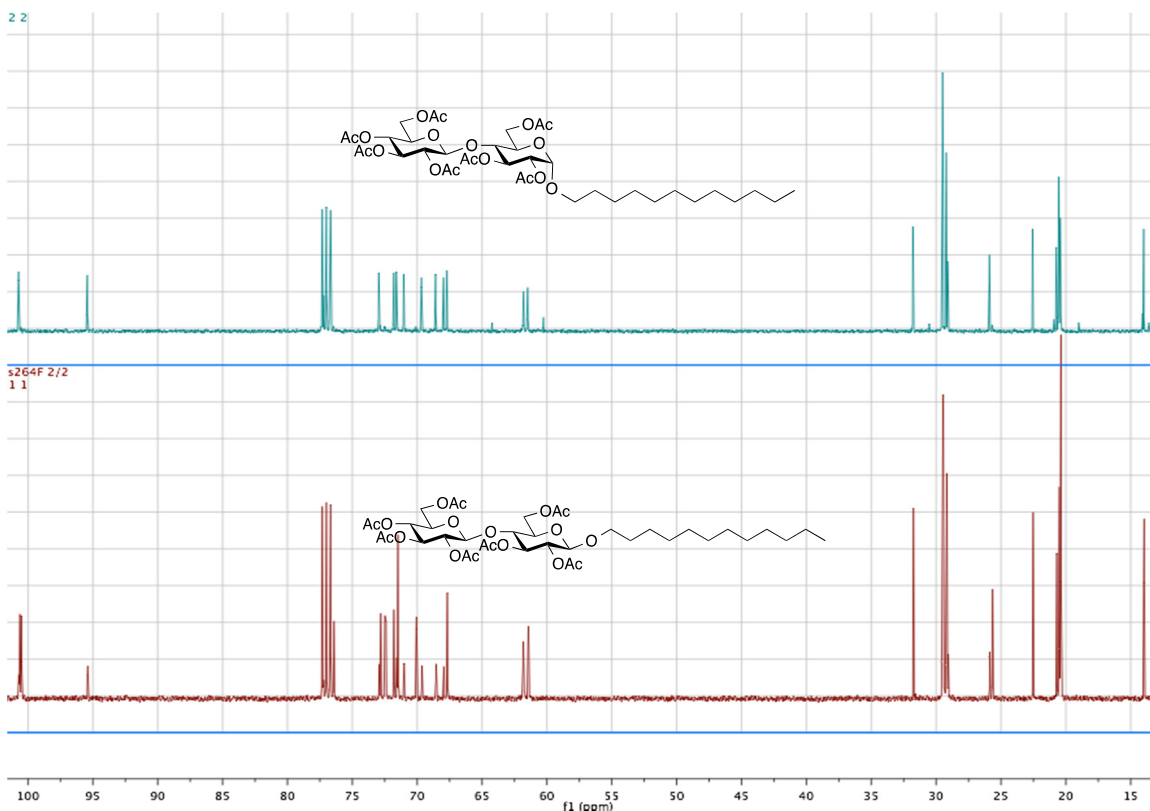


Figure S6d. Expanded ^{13}C -NMR Spectra of Dodecyl-O-acetyl cellobioside (11a)

NMR Spectra of Alkyl-O-Melibiosides (¹H-NMR, Expanded ¹H-NMR, ¹³C-NMR, and Expanded ¹³C-NMR)

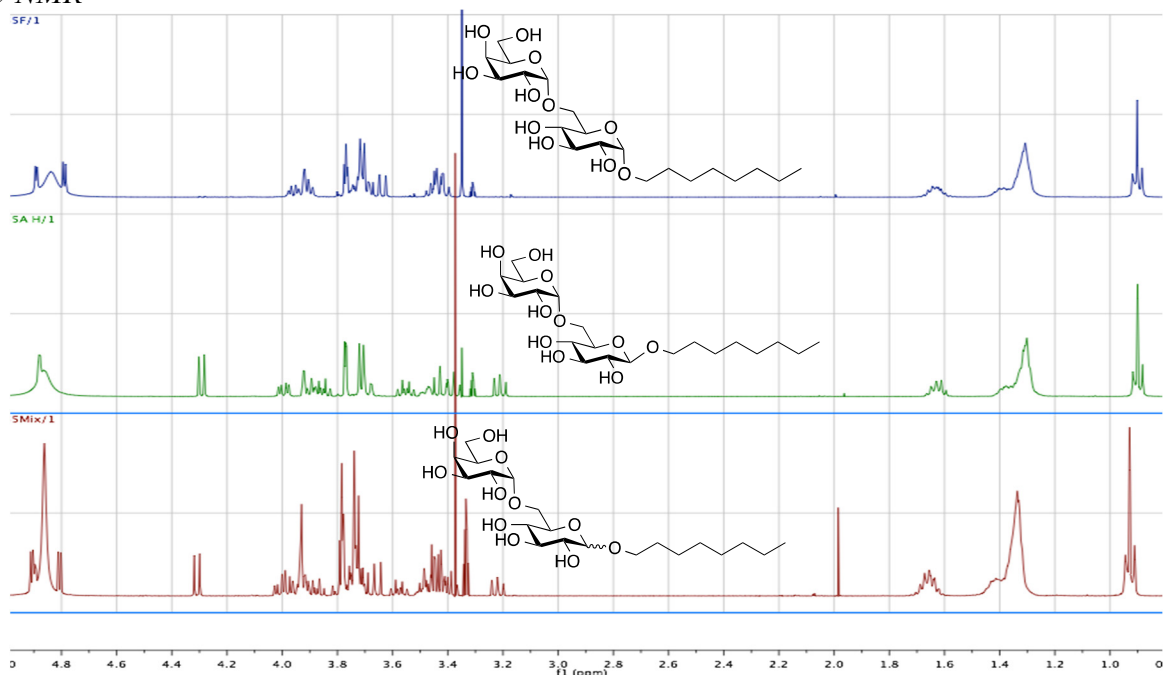


Figure S7a. ¹H-NMR Spectra of Octyl-O-melibioside (6)

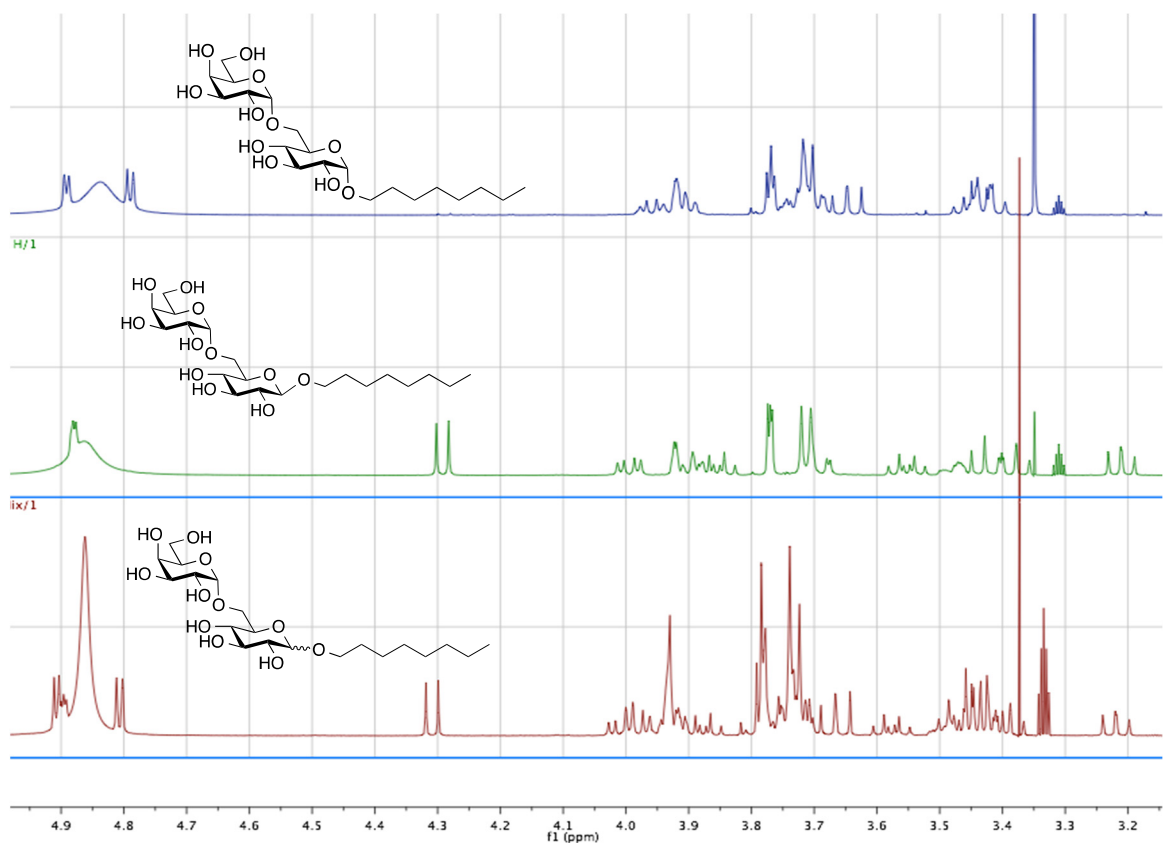


Figure S7b. Expanded ¹H-NMR Spectra of Octyl-O-melibioside (6)

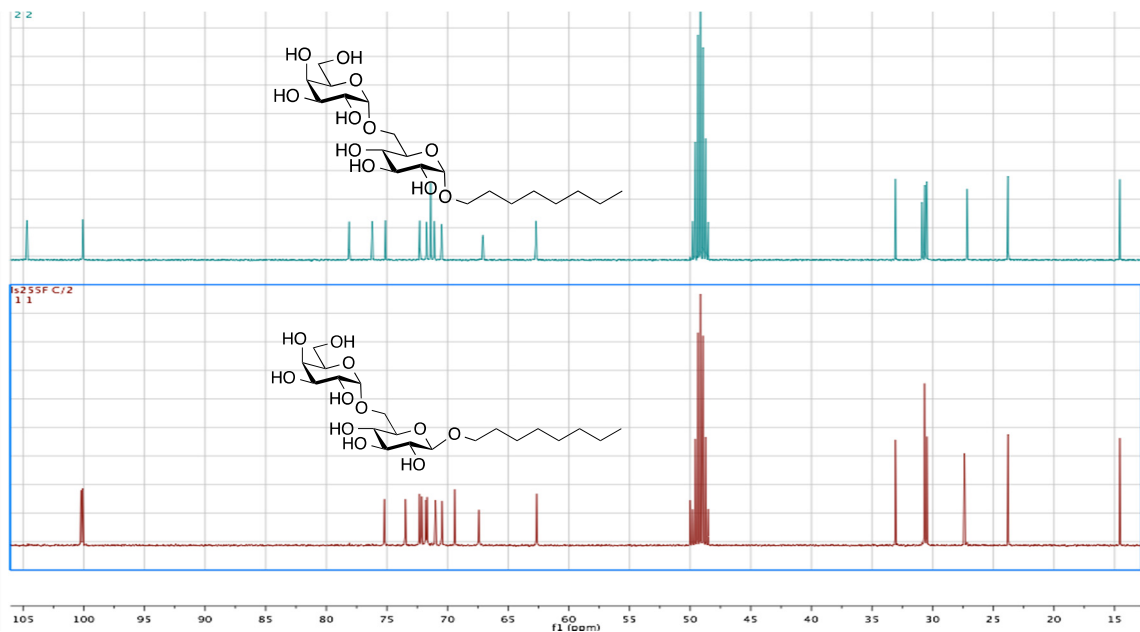


Figure S7c. ^{13}C -NMR Spectra of Octyl-O-melibioside (6)

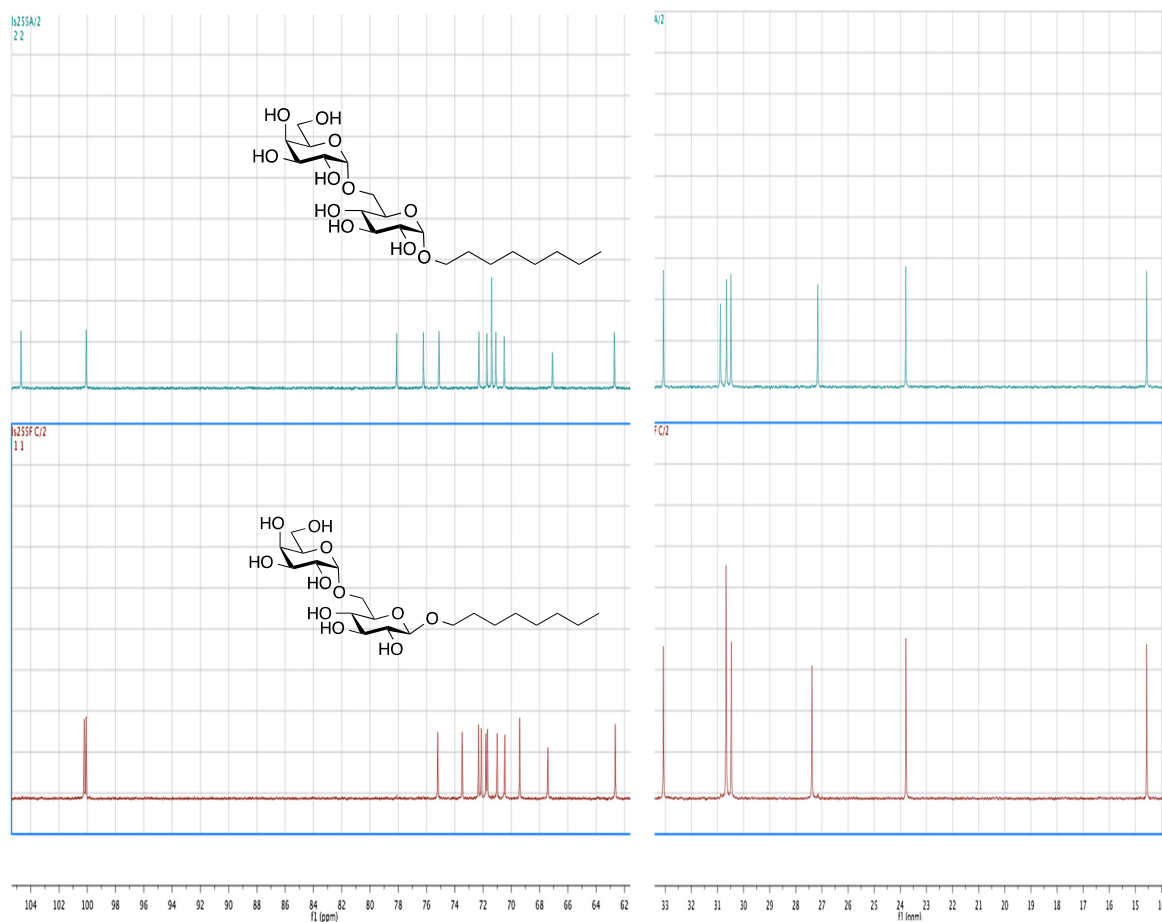


Figure S7d. Expanded ^{13}C -NMR Spectra of Octyl-O-melibioside (6)

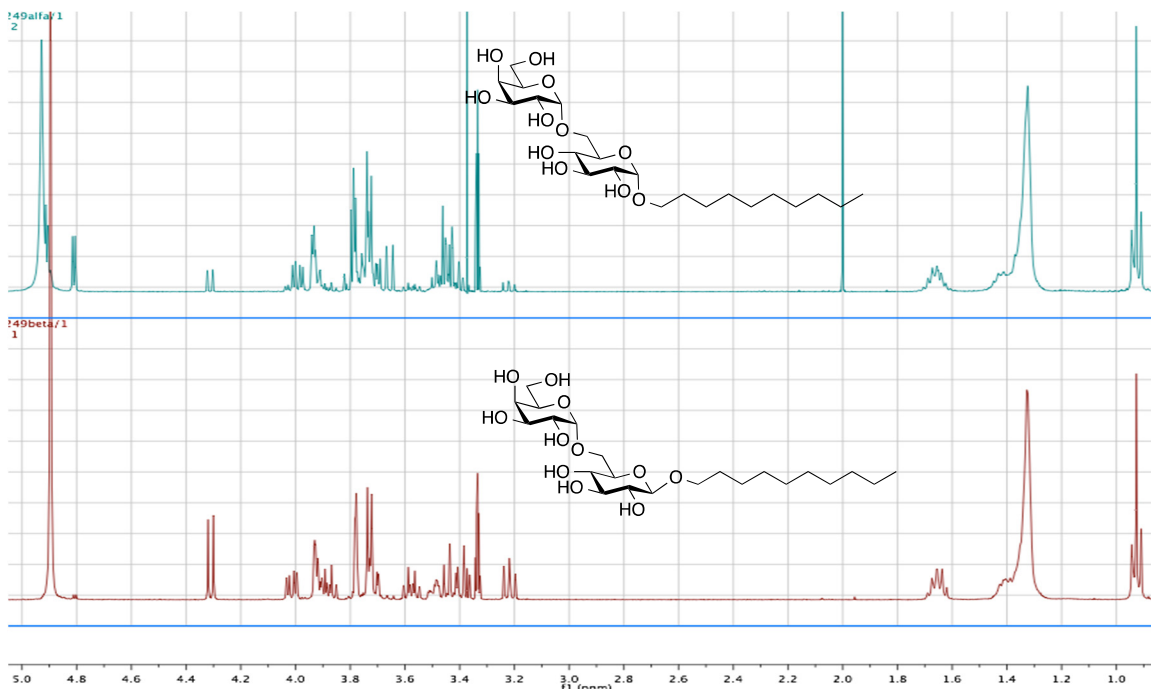


Figure S8a. $^1\text{H-NMR}$ Spectra of Decyl-O-melibioside (7)

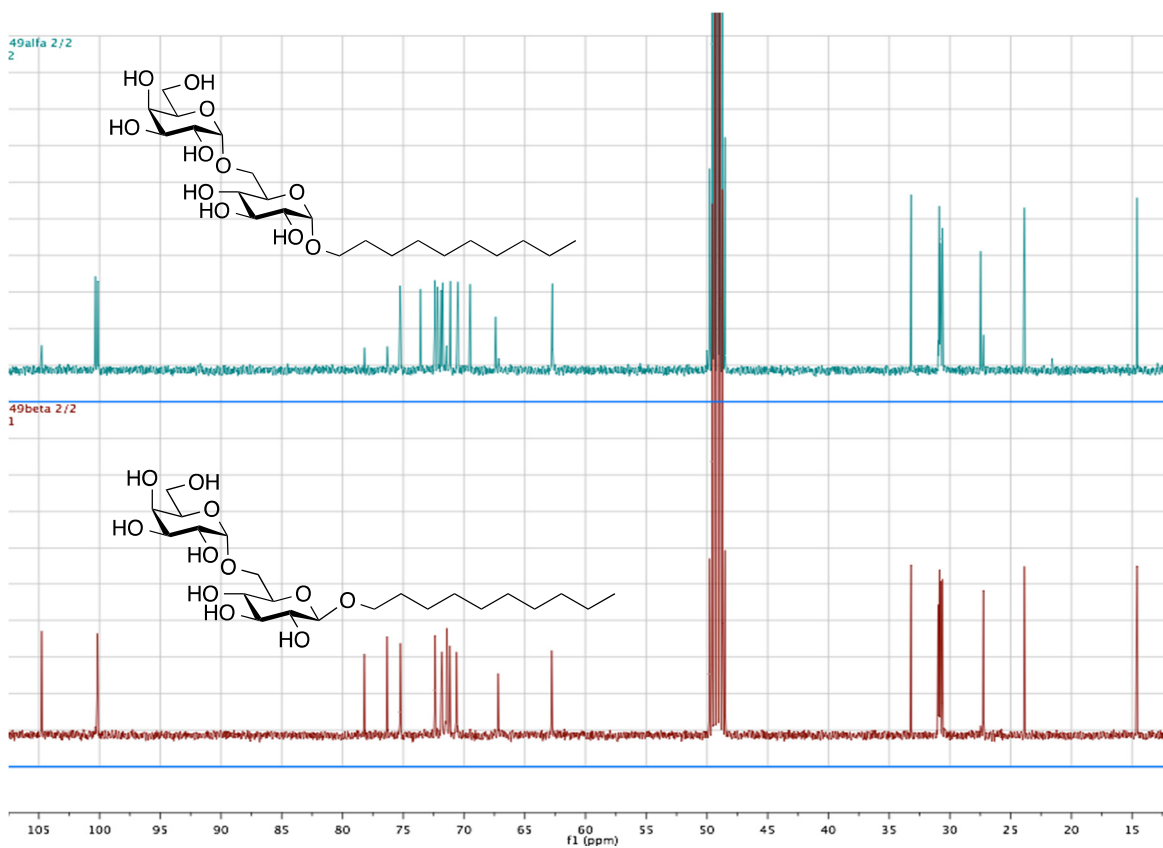


Figure S8b. $^{13}\text{C-NMR}$ Spectra of Decyl-O-melibioside (7)

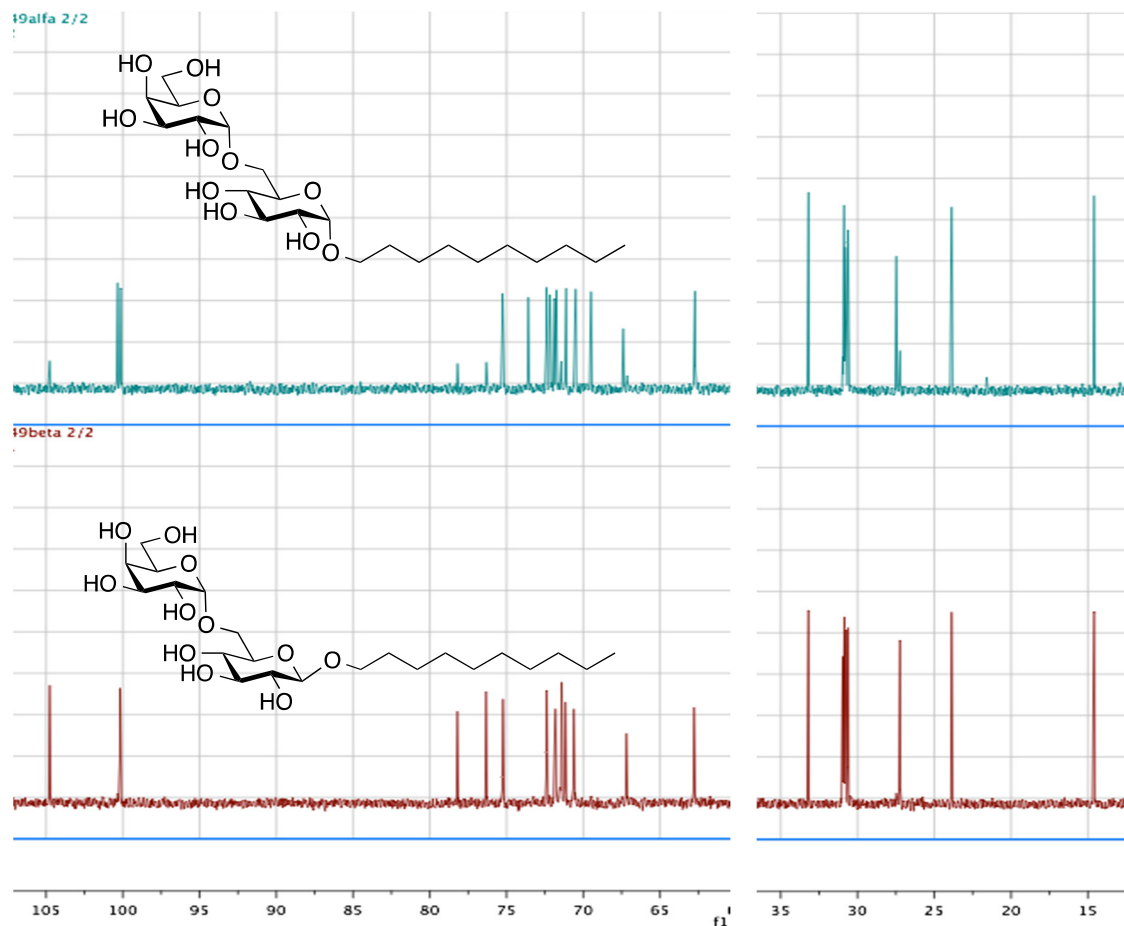


Figure S8c. Expanded ^{13}C -NMR Spectra of Decyl-O-melibioside (7)

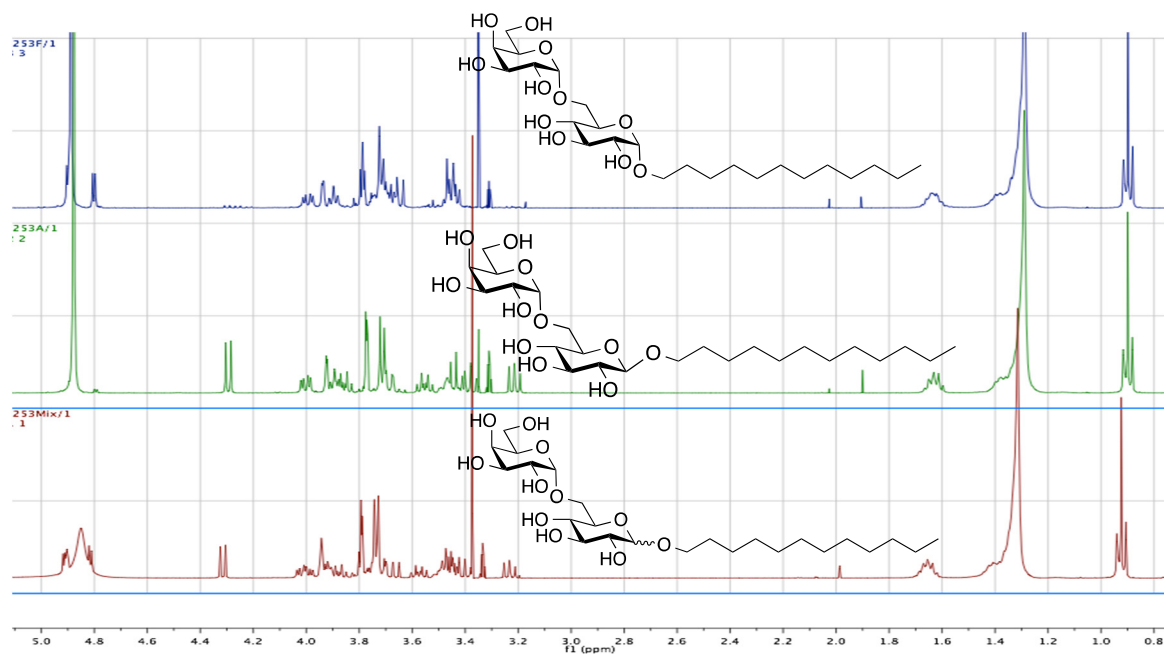


Figure S9a. ^1H -NMR Spectra of Dodecyl-O-melibioside (8)

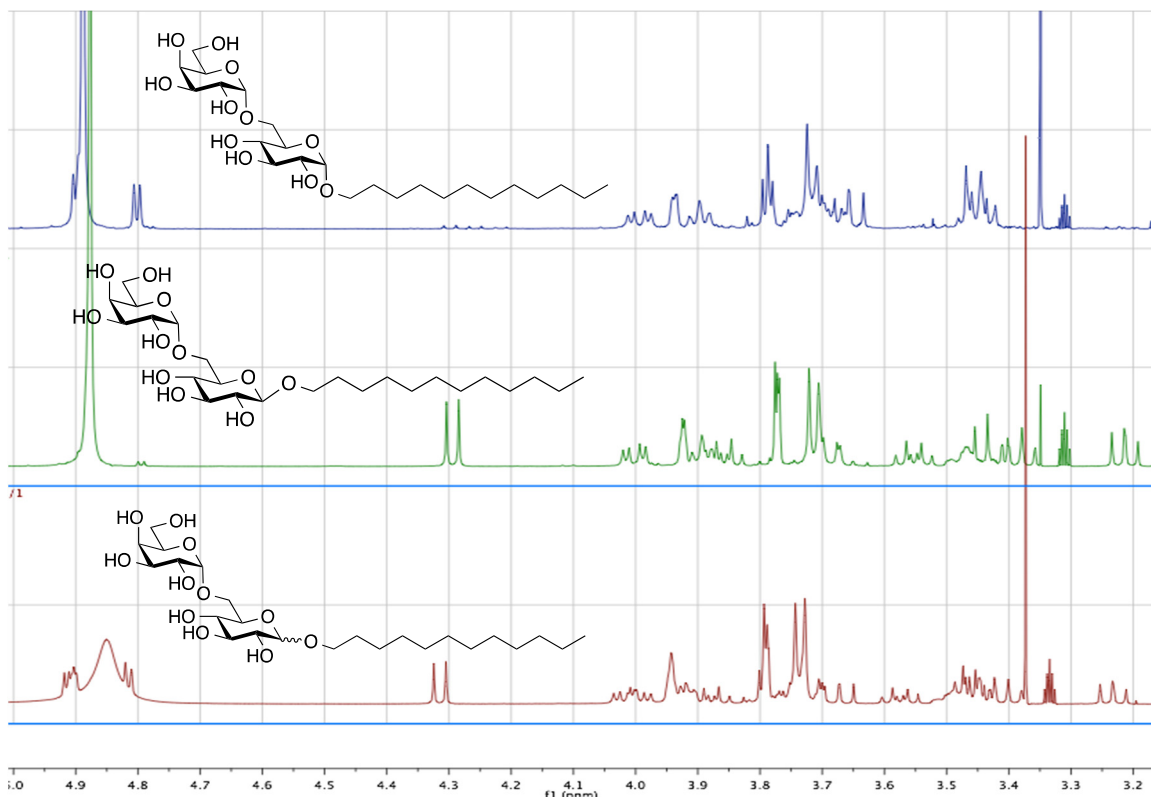


Figure S9b. Expanded ¹H-NMR Spectra of Dodecyl-O-melibioside (**8**)

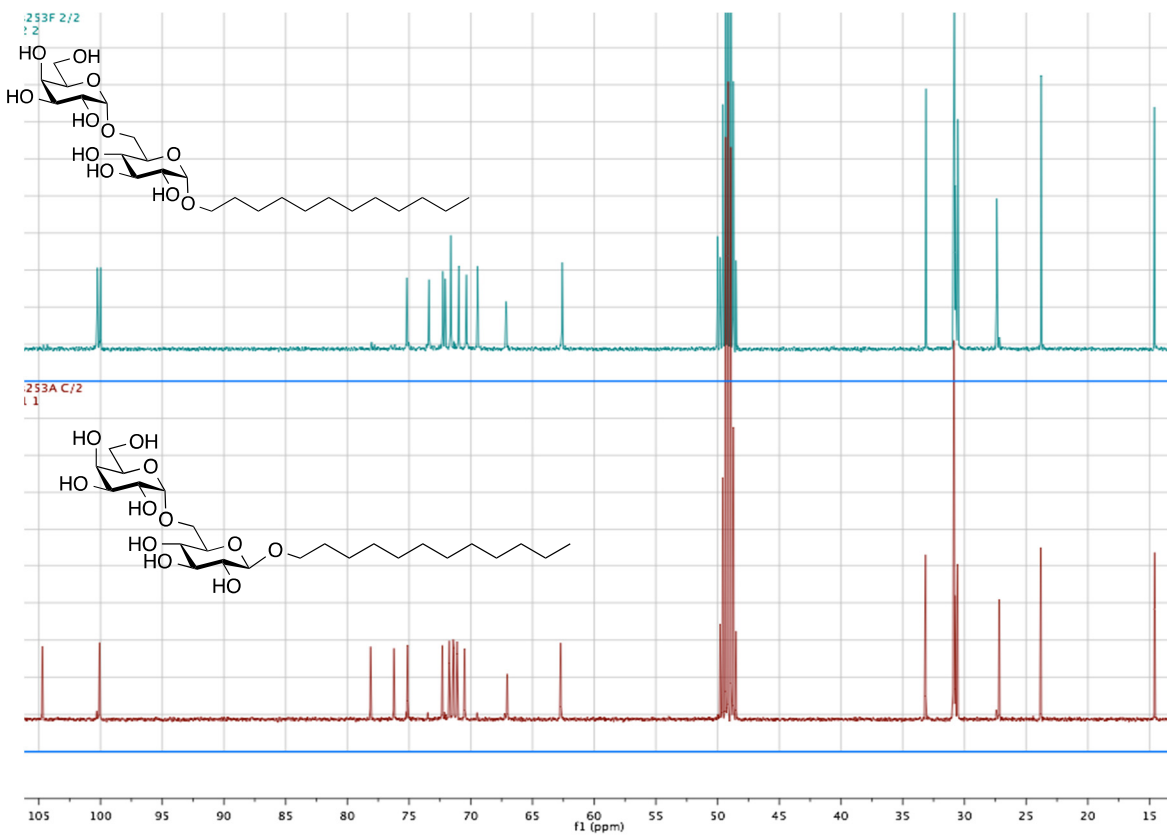


Figure S9c. ¹³C-NMR Spectra of Dodecyl-O-melibioside (**8**)

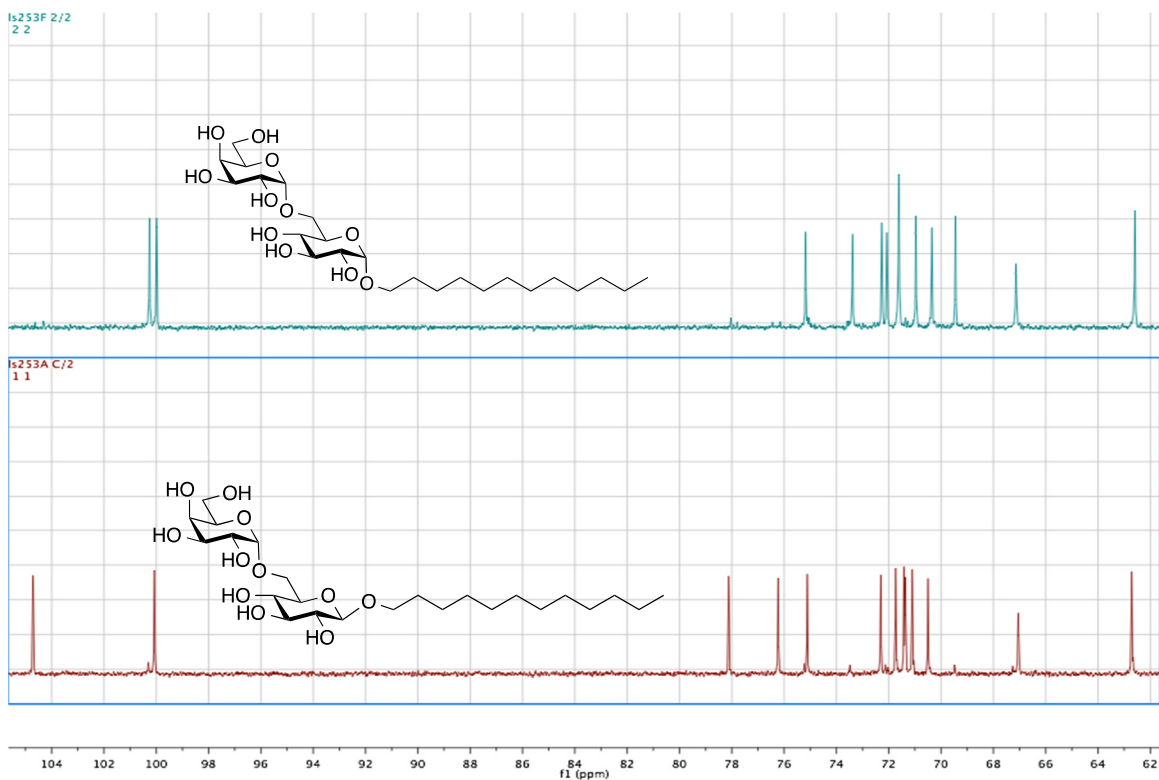


Figure S9d. Expanded ^{13}C -NMR Spectra of Dodecyl-O-melibioside (8)

NMR Spectra of Alkyl-O-Cellobiosides (^1H -NMR, Expanded ^1H -NMR, ^{13}C -NMR, and Expanded ^{13}C -NMR

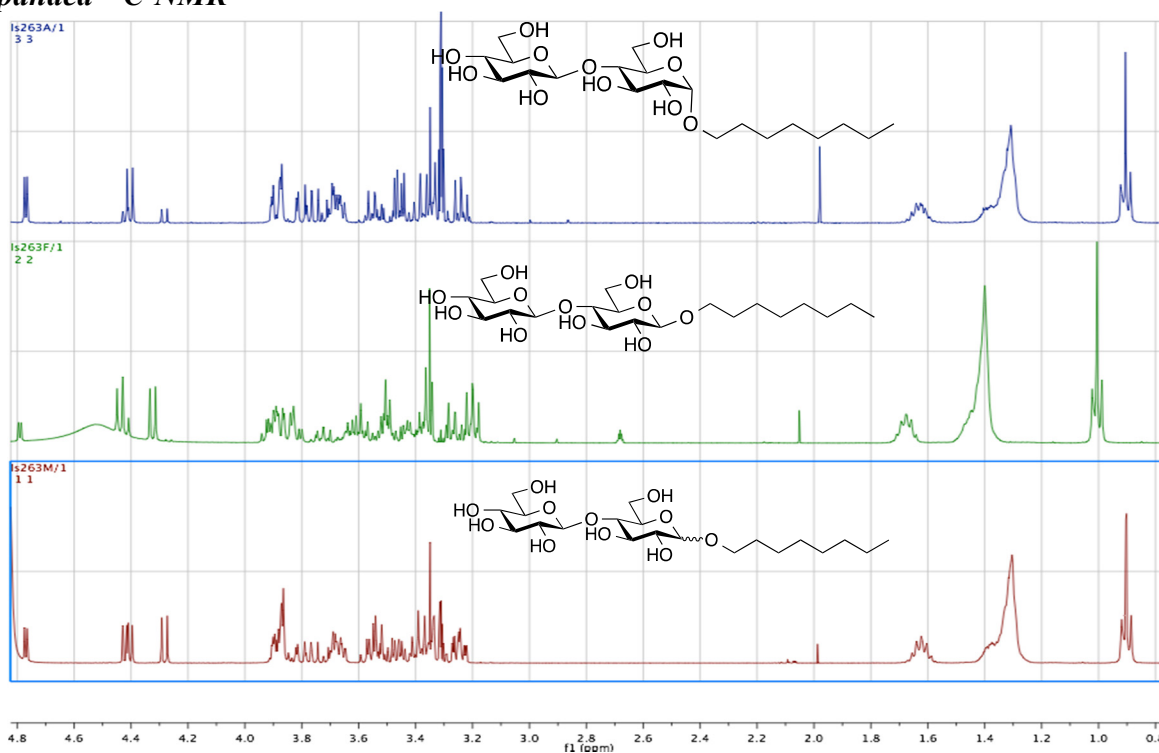


Figure S10a. ^1H -NMR Spectra of Octyl-O-cellobioside (9)

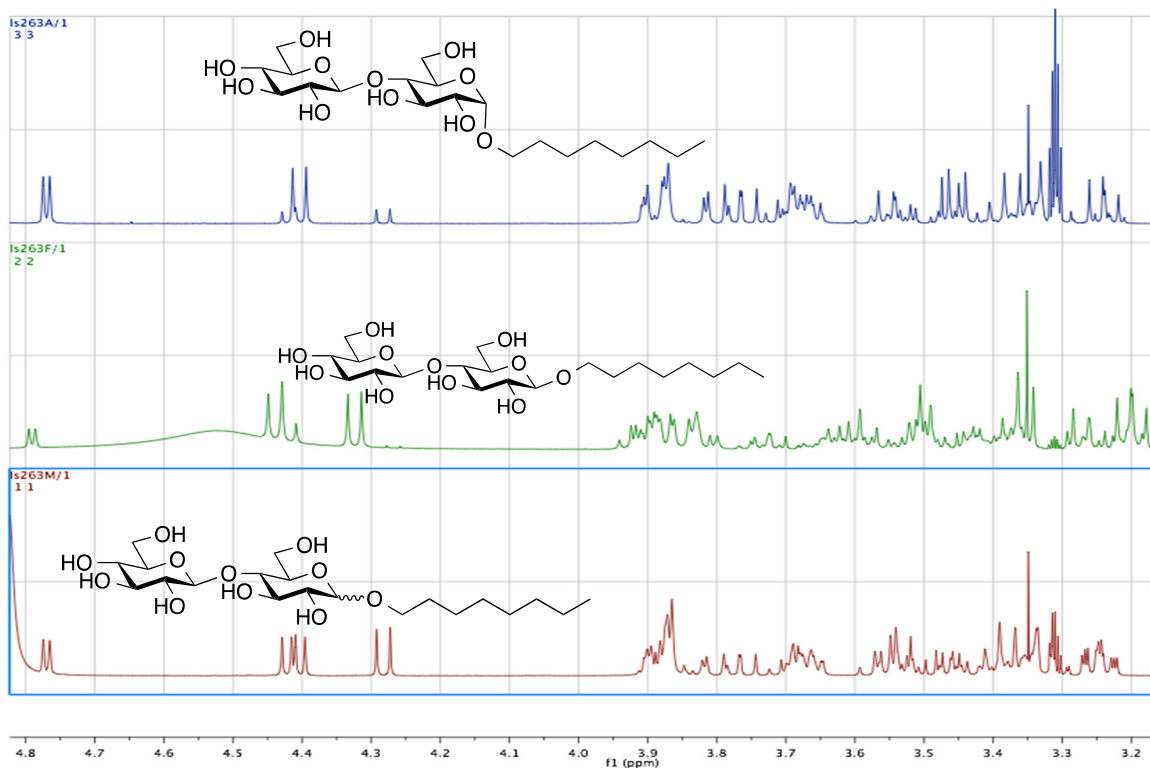


Figure S10b, Expanded ¹H-NMR Spectra of Octyl-O-cellobioside (9)

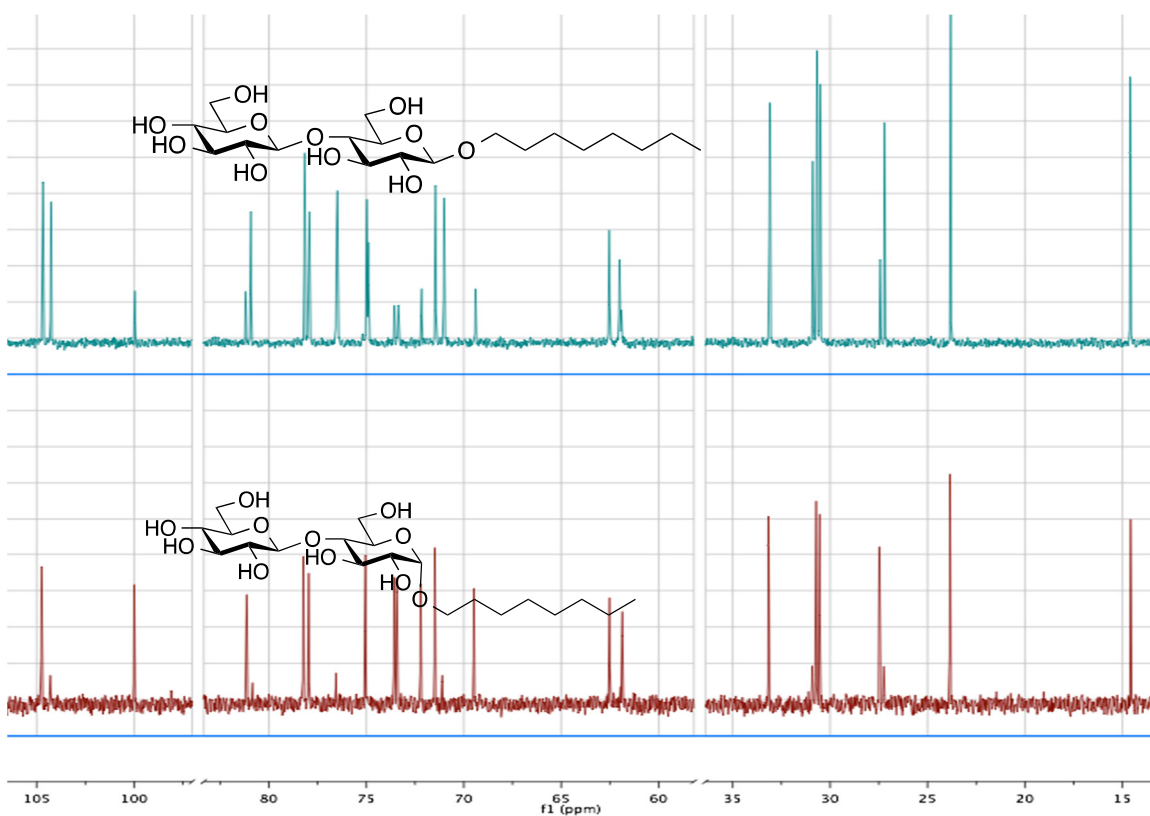


Figure S10c, ¹³C-NMR Spectra of Octyl-O-cellobioside (9)

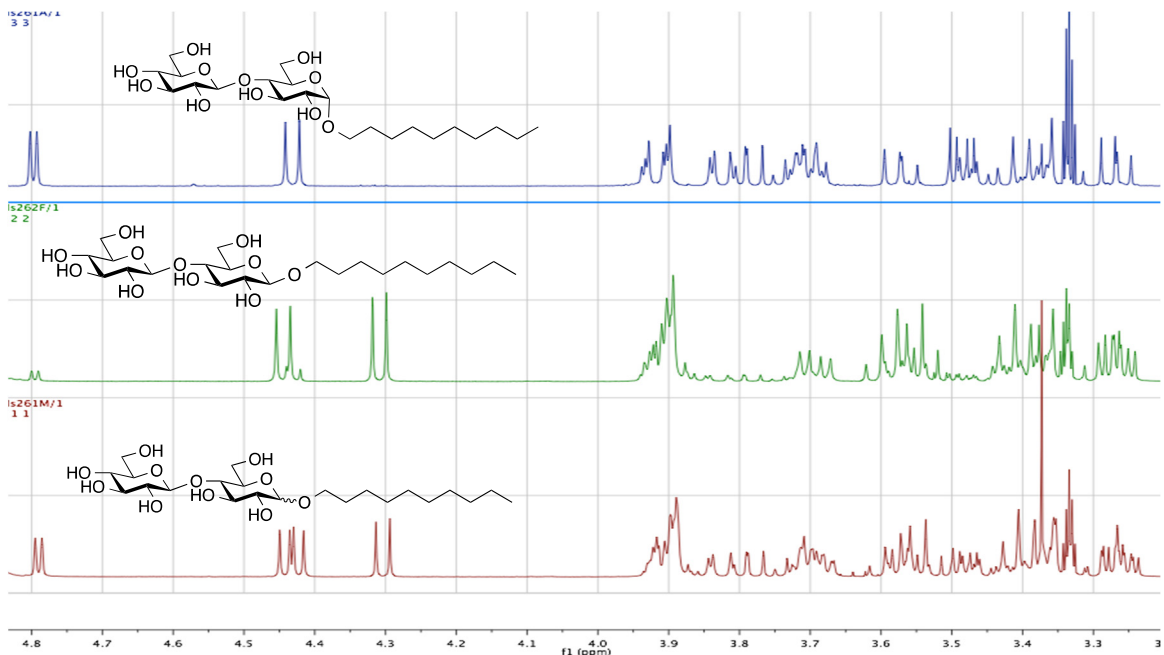


Figure S11a, $^1\text{H-NMR}$ Spectra of Decyl-O-cellobioside (10)

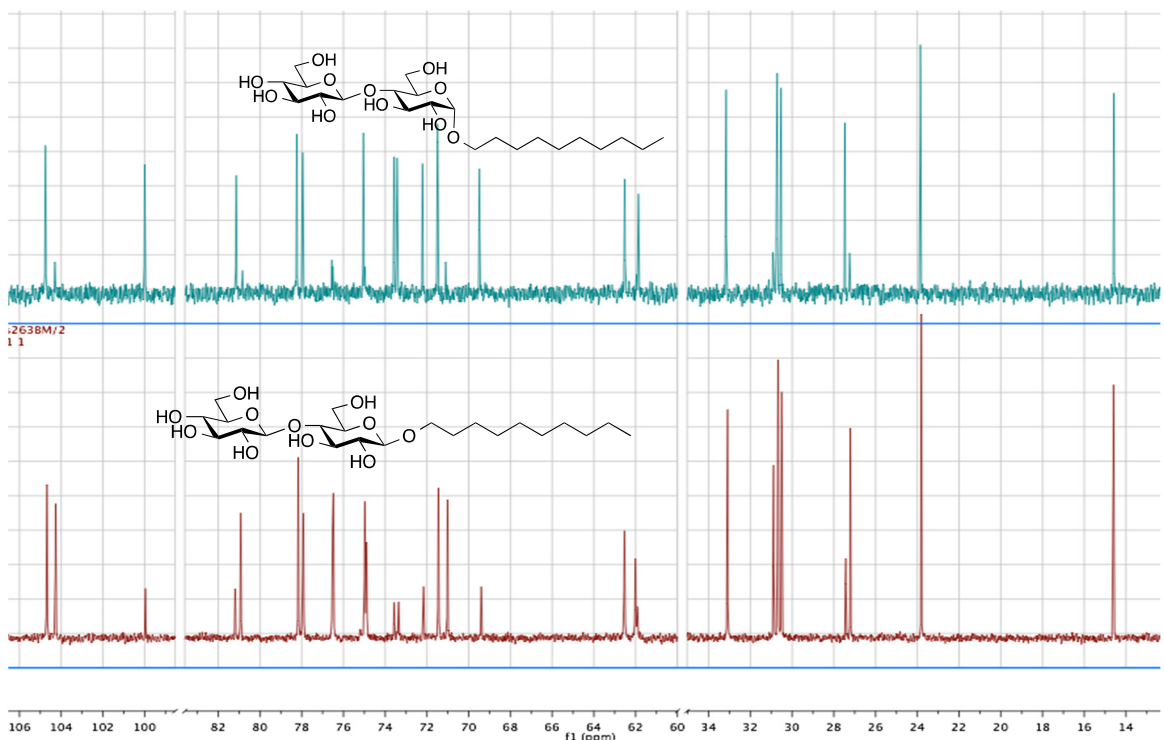


Figure S11b, $^{13}\text{C-NMR}$ Spectra of Decyl-O-cellobioside (10)

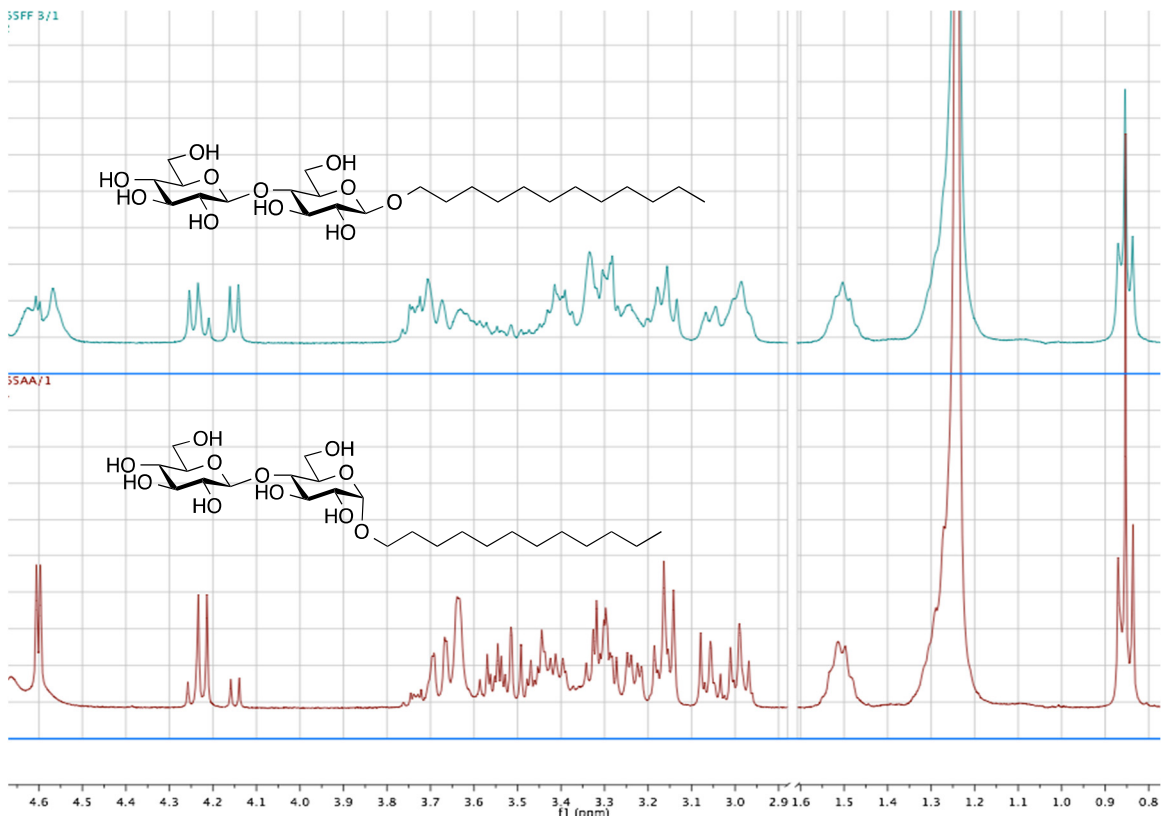


Figure S12a, ¹H-NMR Spectra of Dodecyl-O-cellobioside (11)

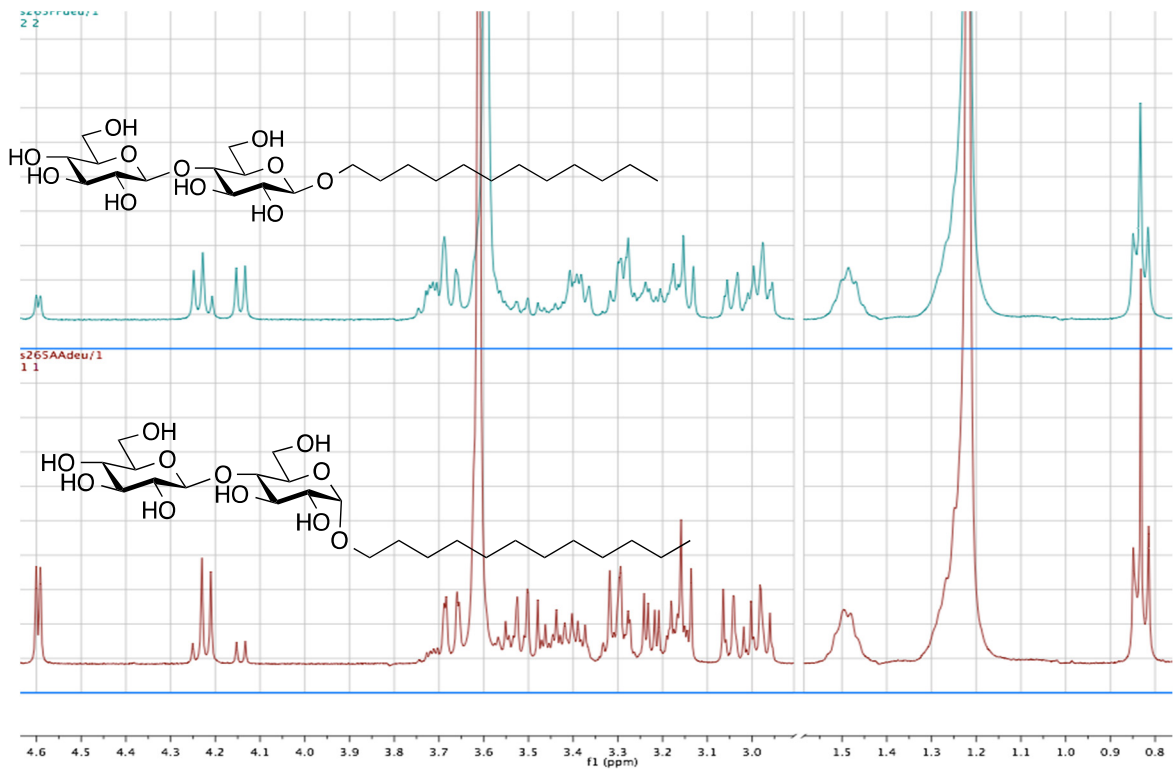


Figure S12b, ¹H-NMR Spectra of Dodecyl-O-cellobioside with D₂O (11)

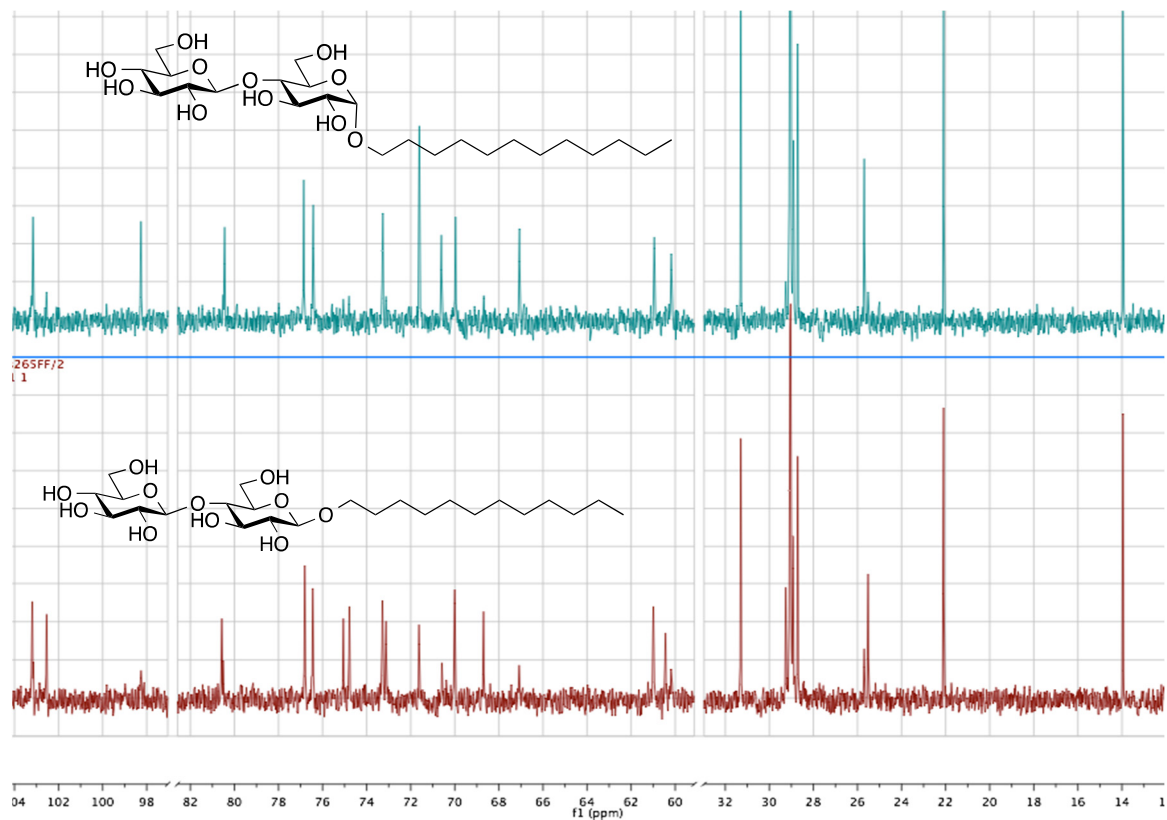


Figure S12c, ^{13}C -NMR Spectra of Dodecyl-O-cellobioside (11a)

Silanization coating procedure for quartz

Quartz fluorescence cuvettes were silanized to preclude surfactant adsorption to the walls. The cuvettes were cleaned in boiling piranha (3 H₂SO₄:1 H₂O₂) for 1 h, then rinsed with nanopure water and placed in a vacuum oven at 120°C overnight. 97.5% v/v dry toluene (ACS grade, EMD, dried over molecular sieves), 0.5% v/v dry pyridine (99.9%, Mallinkrodt), and 2% v/v (tridecafluoro-1,1,2,2-tetrahydrooctyl)triethoxysilane (Gelest) were mixed and stirred for 10 min in a controlled environment hood (purging with Ar and N₂). The silane solution was immediately added to the cleaned, dried cuvettes. The filled cuvettes were allowed to sit in the controlled-environmental chamber for >4 h. After coating, the cuvettes were rinsed with several aliquots of dry toluene followed by several aliquots of absolute ethanol. The coating was cured overnight in a vacuum oven at 100 °C.

LC-MS of glycolipids

LC-MS was performed on several of the glycolipids to observe presence of degradation products and/or impurities. The instrument used was an Acquity iClass UPLC with an Acquity UPLC BEH C-18, 1.7 μm, 2.1 x 50 mm column and detection by Xevo G2-S QTOF (Waters) operated in the negative electrospray ionization mode scanning from 100-1000 Daltons. The mobile phase was 50:50 water:acetonitrile with 0.1% formic acid. The injection volume was 1 μl of ~0.5 mg/mL solution in 50:50 water:acetonitrile. The LOD is in the low ng/mL, so ~0.01% impurity is detectable. No difference from the blank is observed (Figure S13) indicating that these glycolipids are >99.9% pure.

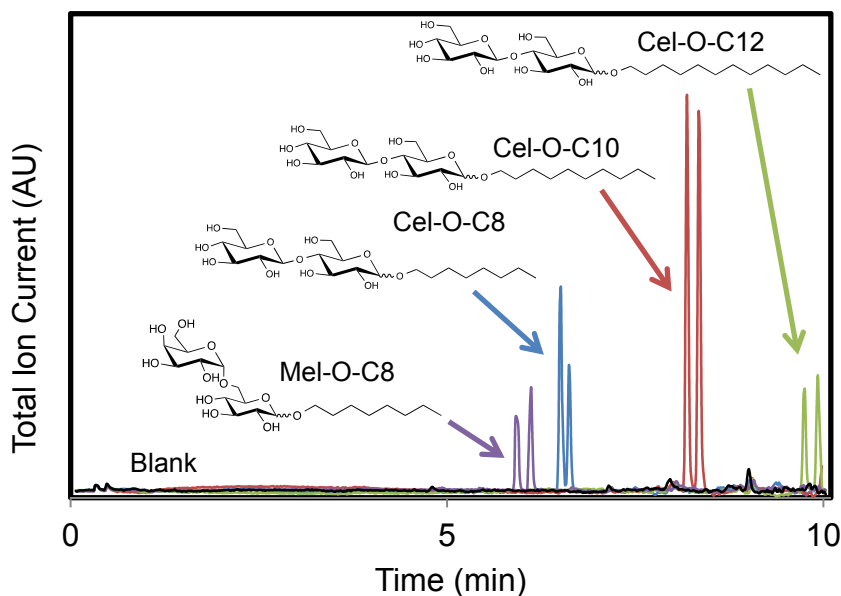


Figure S13. LC-MS of glycolipids. Two peaks are present for each glycolipid arising from the different anomers, with the α : β ratio \sim 50:50.

DLS distribution transformations

The DLS distribution transformations from the measured intensity ($\%I_i$) to concentration/mass ($\%C_i$) to number ($\%N_i$) have several inherent assumptions that may skew the analysis if used rather than the $\%I_i$. The $\%C_i$ and $\%N_i$ are calculated from $\%I_i$ as follows;

$$\%C_i = I_i / (R_i^x k^y) \div \sum I_i / (R_i^x k^y) \times 100\% \quad [1]$$

$$\%N_i = I_i / (R_i^{2x} k^y) \div \sum I_i / (R_i^{2x} k^y) \times 100\% \quad [2]$$

where x is a shape factor, R_i is the radius of aggregate i , and k^y is a constant that is proportional to the partial specific volume of the aggregate i . k^y cancels out if similar for all i aggregates. The largest assumption in the transformations is that the shape factor represents a sphere ($x = 3$), whereas the aggregates may deviate largely from spherical, e.g. wormlike micelle or lamellae. A shape factor of $x = 2$ represents a rod. A representative DLS distribution (given R_H and $\%I_i$) was analyzed to compare differences in $\%C_i$ and $\%N_i$ induced by the assumption $x = 3$ if indeed $x = 2$ is a better representation for the larger aggregates (Table S5). The most drastic difference in $\%N_i$ is observed for the largest aggregate, $\%(x = 2) / \%(x = 3) = 10^4$ for a rod shaped aggregate. The

$\%N_i$ of the smaller aggregates remains fairly unchanged regardless of shape; however, the $\%N_i$ of the larger aggregates is substantially affected. This leads to DLS analysis with unknown x where the R_H is best represented by intensity distribution and a qualitative statement that if micelles are observable in the DLS results (LOD 0.1 $\%I_i$), they are the predominant aggregate by several orders of magnitude. Also, complications of water within vesicles for the mass model causes a change in $\%N_i$ by another order of magnitude.¹

Table S5: Difference (represented as ratio of $\%(x = 2) / \%(x=3)$) in $\%C_i$ and $\%N_i$ from representative $\%I_i$ vs. R_H data for $x = 2$ (rod) vs. $x = 3$ (sphere).

R_H (nm)	$\%I_i$	$\%(x = 2) / \%(x = 3)$	
		$\%C_i$	$\%N_i$
2	0.1	7.E-01	1.E+00
50	30	2.E+01	6.E+02
300	69	1.E+02	2.E+04

Derivation of simplified Infelta-Tachiya equation (negligible Q, P migration and solubilization in aqueous solution)²⁻⁵

Fluorescence intensity decay depends on the fluorescence lifetime (τ_0) and the quenching rate (k_q), and k_q depends on the number of quencher molecules solubilized within a micelle (n). Micelles act as discrete sub-environments causing a distribution of n across the micelles. Therefore, the intensity at time = t ($I(t)$) is equal to the sum of $I_n(t)$ for all n :

$$I(t) = \sum_{n=0}^{\infty} I_n(t) = \sum_{n=0}^{\infty} I_n(0) \exp(-t/\tau_0 - nk_q t) \quad [1]$$

The distribution of quenchers is described by a Poisson distribution, such that:

$$I_n(0) = I(0) \frac{\langle Q/M \rangle^n}{n!} \exp(-\langle Q/M \rangle) \quad [2]$$

where $\langle Q/M \rangle$ is the average quencher to micelle concentration ratio ($[Q]/[M]$). Combining equations [1] and [2] leads to:

$$I(t) = I(0) \sum_{n=0}^{\infty} \frac{\langle Q/M \rangle^n}{n!} \exp(-\langle Q/M \rangle) \exp(-t/\tau_0 - nk_q t) \quad [3]$$

The reduced form is the familiar Infelta-Tachiya equation:

$$I(t) = A_1 \exp[-A_2 t - A_3 (1 - \exp(-A_4 t))] \quad [4]$$

where $A_1 = I(0)$, $A_2 = 1/\tau_0$, $A_3 = [Q]/[M]$, and $A_4 = k_q$. Equation [4] may be fit to TRFQ decay curves to solve for the fitting parameters $A_2 - A_4$ with A_1 determined from the maximum intensity.

Assumptions for use of simplified Infelta-Tachiya equation

Several assumptions are inherent to equation 1, and should be adequately supported in order to substantiate use of this analysis. The model for quenching within micelles must be chosen carefully for assessing various assumptions as follows:^{3,5-13}

- 1) P and Q occupancy follow a Poisson distribution where maximum occupancy is ∞ .
- 2) $k_q/k_f > 1$ where k_f is the fluorescence rate ($1/\tau_0$).
- 3) Micelles are relatively monodisperse ($\sigma < 50\%$) and small ($N_{agg} < 500$).
- 4) Q and P are solubilized primarily in the micelle.
- 5) P residence time is $\gg \tau_0$. (Note that migration of quencher is included in equation 1.)
- 6) Static quenching contributions are minimal.

Assumption 1) is upheld for $[\text{solute}]/[M] < 2$.^{3,5,12,13} Assumption 2) generally follows for a long fluorescence lifetime (pyrene $\tau_0 > 300$ ns in micelles^{9,14}), most monomeric (non-gemini) aqueous micelle solutions,¹⁵ and may be self-validated by the TRFQ results. Assumptions 3)-6) should be individually addressed for the particular system under investigation. Polydispersity skews N_{agg} and k_q as the solubilizes preferentially load into larger micelles, but negligible polydispersity may be validated by $dN_{agg}/d[Q] \sim 0$.^{7,16} or analysis of the distribution of lifetimes¹⁷. Furthermore, the quenching kinetics in larger aggregates, such as vesicles, tend toward homogeneous solution rather than equation [1] and are observed by a significant $d(A_4/A_{4,min})/d[Q]$.¹⁰ The presence of vesicles should be considered in this way, but cylindrical shape effects on solubilize diffusion and quenching kinetics are negligible for probes with long lifetimes (>50 ns) in micelles with $N_{agg} < 500$.¹⁸ Significant partitioning of quencher and/or probe between aqueous and micellar phases may cause deviations from equation [1],⁵ but has negligible effects when the partition coefficient, K , is $>10^4$. This can be evaluated based on the micropolarity of the micelle as indicated by τ_0 in several ways. First, K is $>10^4$ if the system is more hydrophobic than SDS as determined by relative τ_0 ($\geq \tau_{0,SDS} = 321 \pm 7$ ns), because in aqueous SDS, the K_{pyrene} is 8.9×10^5 and $K_{\text{benzophenone}}$ is 1.2×10^4 (using octanol water partitioning from the CODATA Canada

database¹⁹).²⁰ Secondly, the lifetime of the probe is much shorter in water, so observation of $\tau_{0,\text{micelle}} \gg \tau_{0,\text{aqueous}}$ corroborates primary residence in the more hydrophobic surfactant aggregates; a single exponential fit (i.e. single τ_0) without quencher also indicates residence in a single domain. The next assumption regards skewing of the statistical model by solubilize migration between micelles on the scale of the fluorescence lifetime ($k_{-} > k_f$).^{21,22} The migration is calculated from equation [1], and the similarity between $1/A_2$ and τ_0 also serves as validation of negligible migration ($1/A_2 = \tau_0$ when $k_{-} = 0$). For a more hydrophobic probe than quencher, the probe migration must only be assessed if $k_{-} > k_f$.^{8,21-23} Lastly, static quenching contributions may reduce the [Q] available for dynamic quenching and deviate the kinetics from equation [1].^{8,11} However, the benzophenone-pyrene quenching mechanism is a diffusion-limited collisional electron transfer.²⁴ Therefore, only pseudo-static quenching on the scale of the lifetime ($k_q \sim k_f$) requires consideration, and this sort of effect is minimal for pyrene and benzophenone in SDS.¹¹ The assumptions are validated accordingly in the presented analysis.

Further details on polydispersity analysis

The measured N_{agg} will depend on the concentration of quencher ([Q]) if the aggregates are polydisperse. At low [Q], the Q loads into the aggregates representing the greatest monomer mass first. If 10% of the aggregates are small unilamellar vesicles (SUV) and 90% are micelles, then there are $\sim 10^3$ times more monomers in the 10% SUV than the micelles, which makes this a feasible observation at low [Q], and is discussed at length in the main text. Conversely, the effects of greater hydrophobicity in the SUV are minimal, because a severe overestimate represented by the solubility of pyrene in cyclohexane compared to methanol only shows a 10x increase. However, another coinciding potential complication was investigated here; the preferential mass loading of the fluorescent probe (P) in addition to the quencher (Q) into the aggregates representing the greatest monomer mass first (number of P and Q is proportional to N_{agg}). The derivation of the Infelta-Tachiya equation involves the summation of all aggregate subsets of particular N_{agg} , number of P, and number of Q, and the Poisson distribution remains valid for each aggregate subset. Thereby, [Q] tending toward the $N_{\text{agg},Q}$ limit ensures that smaller N_{agg} populations (i.e. micelles) are indeed probed.¹⁶ However, the lifetime assessment of the pyrene fluorescence may be skewed to the vesicle populations, if present. To investigate the effects of preferentially probing the larger aggregates, the fluorescence lifetime of pyrene at 1

and 5 μM in 31.5 mM Cel-O-C8 ($[\text{P}]/[\text{S}]_{\text{m}} = 0.00008$ and 0.004) was measured. This represents a population with perceptible vesicle contributions. There was no statistical difference observed for the lifetime at $[\text{P}] = 1$ and $5 \mu\text{M}$ (340 ± 17 ns and 336 ± 4 ns) where skewness effects would be large. Greater $[\text{P}]$ was prohibited by increasing the proportion of greater than single P occupancy and subsequent excimer formation. In this way, a single exponential fit to data without quencher was appropriate in all instances. Furthermore, no statistical difference in N_{agg} was observed for varying $[\text{P}]$ (2 and $5 \mu\text{M}$) with constant $[\text{Q}]$ (0.532 mM) and $[\text{S}]$ (31.5 mM Cel-O-C8); 22 ± 5 and 28 ± 3 molecules/micelle. The preferential loading of P into larger aggregates is not considered significant to this study.

For the systems studied, a significant population of vesicles is present in each case in which polydispersity is indicated. Thus, although the micelle size may exhibit some dispersity, the skew in the data arises primarily from this small population of vesicles with drastically larger N_{agg} . The measured polydispersity reflects an average N_{agg} distribution peak; therefore, the measured single distribution peak will appear to have positive skew if the distribution is two discrete populations (a smaller peak at high vesicle N_{agg} and a larger peak at low micelle N_{agg}). If the skew is solely attributable to the presence of the vesicle population and the RSD is negligible for the TRFQ analysis, N_{agg} at high $\langle Q \rangle$ would be representative of the micelle population. The significance of bias imposed by both vesicle presence and RSD should be assessed separately.

Anomeric effect on energy-minimized structure

The glycolipids studied are a 1:1 ($\pm 2\%$) anomeric mixture of $\alpha:\beta$, and the differences in the stereochemistry should be considered when analyzing the mixture characteristics. As an example, the energy minimized molecular mechanics structures from Chem 3D are shown in Figure S14 for Mel-O-C10 and Cel-O-C10. Similar effects are observed for the octyl and dodecyl chains as well.

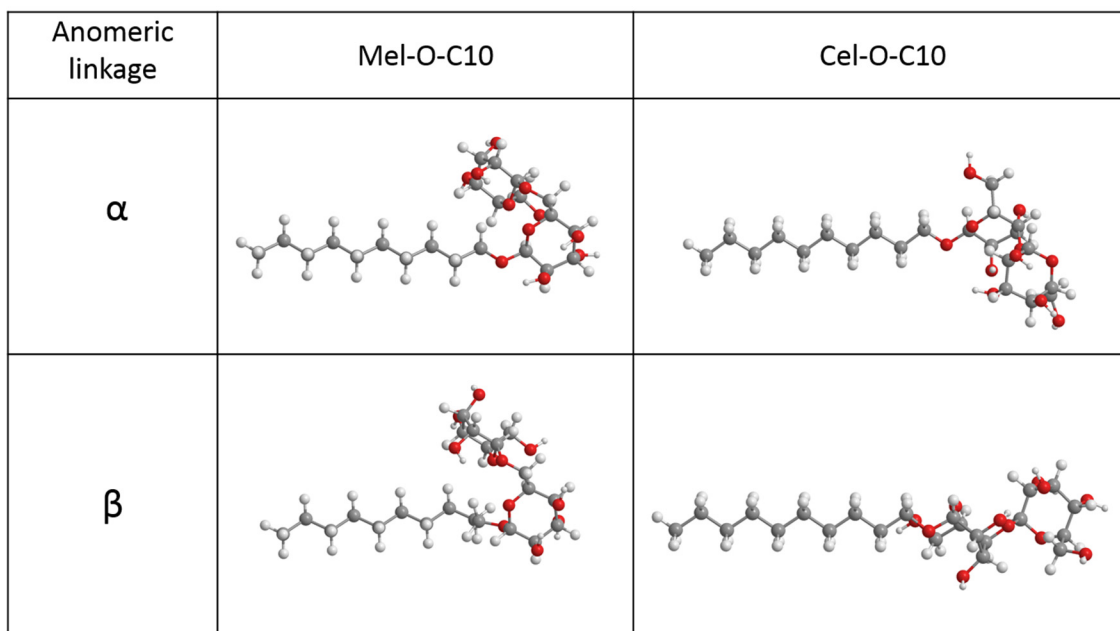


Figure S14. Energy-minimized molecular mechanics structures of anomers of n-decyl-O- β -cellobioside and n-decyl-O- β -melibioside.

CMC curves determined by tensiometry and fluorescence spectroscopy

Surface tensiometry measurements were taken on each glycolipid anomeric mixture as well as the pure anomers of Mel-O-C10 as shown in Figure S15. The Cel-O-C12 solubility is $\sim 250 \mu\text{M}$; therefore, the concentrations $>250 \mu\text{M}$ are representative of the amount of the compound per unit volume of the aqueous mixture.

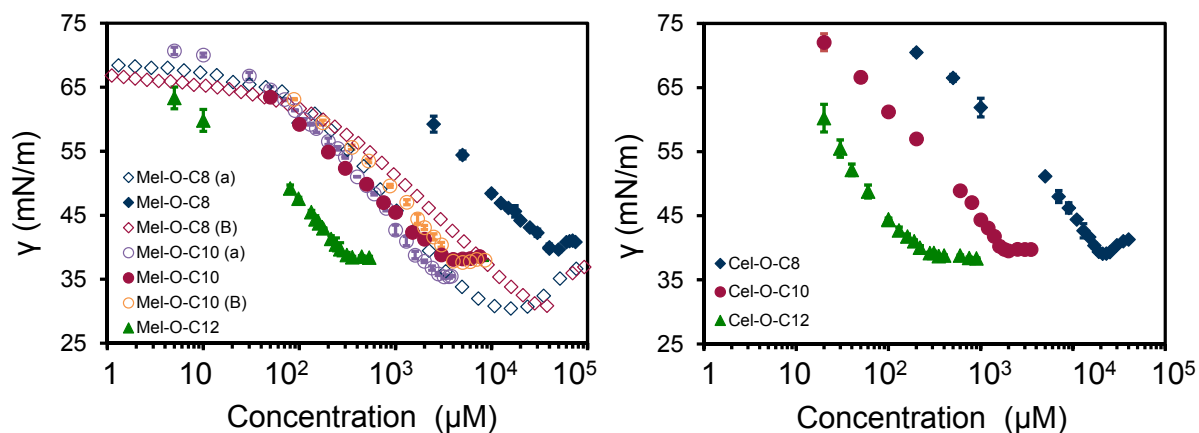


Figure S15. Surface tensiometry curves of alkyl melibiosides and alkyl cellobiosides. Note: data presented for Mel-O-C8 pure anomers represent single measurements due to the small amounts available; data for all other systems represent an average of triplicate measurements.

The tensiometry data for the octyl chain glycolipids exhibit minima in surface tension values in the vicinity of the CMC, which may arise from the presence of trace impurities. Neither NMR (purity >98%, see Figures S1-S12) nor LC-MS (purity >99.9%, see Figure S13) data indicate the presence of impurities or degradation products; therefore, it is unlikely that these minima are caused by surface-active impurities. As discussed in the main text, the anomers exhibit different surface activities; thus one possible explanation for these minima is that they are due to a disparity in anomer activity. More complex adsorption processes and possible transformations in packing structure at the air-water interface may also contribute to these minima.^{36,41,42} Nonetheless, the minima are pertinent to this discussion for their potential effect on the measured CMC values; therefore, the CMCs have been validated by fluorescence spectroscopy.

The potential effect of this minimum on the determination of the CMC was evaluated by comparison to the CMC calculated from fluorescence spectroscopy (Figure S16). The change in pyrene fluorescence properties with surfactant concentration is widely used as an indicator of CMC.²⁵ Namely, the pyrene monomer fluorescence lifetime, τ_{avg} , increases upon micellization. Solutions were prepared with 5 μM pyrene, and the fluorescence lifetime was measured as described in the experimental section for 15 to 81 mM Mel-O-C8. In addition to indicating polarity ($\tau_0 = 200$ ns in water and $\tau_0 = 330\text{-}350$ ns in Mel-O-C8), pyrene also forms excimers with a drastically lower lifetime (~ 45 ns) when present at $>\mu\text{M}$ concentrations in water.^{26,27} At 5 μM pyrene and surfactant concentrations above the CMC, the pyrene molecules are isolated in micelles which increases the the pyrene monomer lifetime. At 5 μM pyrene and surfactant concentrations below the CMC, pyrene senses a more hydrophilic environment, which reduces the monomer lifetime; additionally, excimers may be formed as well. The CMC is calculated from the monomer lifetime vs. concentration data according to the procedure outlined by Aguiar et al.²⁸ The CMC is 35 ± 4 mM and is statistically similar to the CMC by tensiometry (44 ± 5 mM), which verifies that the surface tensiometry is not significantly affected by the presence of the minimum. Furthermore, the region for micellization (approximately 30 to 45.5 mM) is relatively wide, indicating coexistence of premicelles and micelles, rather than a rapid point of full micellization. In this regard, the CMC may be considered as 45.5 mM. Thus, although a minimum in surface tension past the CMC is evident, it has minimal effect on the CMC and most likely arises from restructuring of the surfactant at the air-water interface.

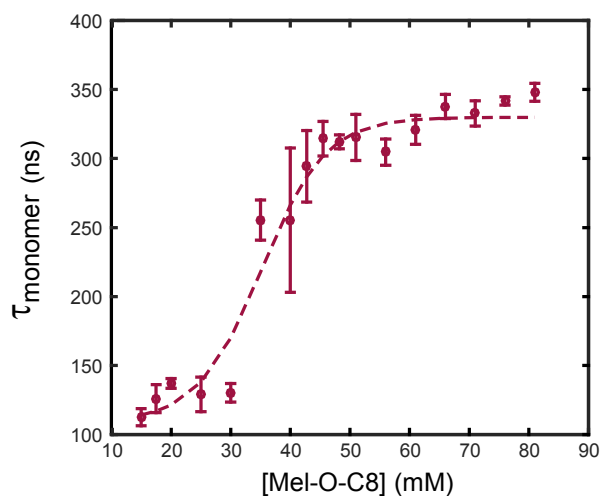


Figure S16. Mel-O-C8 CMC determination from pyrene monomer fluorescence lifetime as a function of concentration (\bullet). CMC is determined as the inflection point of the Boltzmann sigmoid fit to the data (---).

Representative TRFQ data and fitting procedures

TRFQ spectra with and without quencher were fit with equation [4] as described in the main text with additional details below. A representative curve is shown below in Figure S17. The fitting is performed on the data region from seven pixels past $I(0)$ ($t = 13.7$ ns) to the pixel where S/N decreases to ~ 5 (typically at $I(t) \sim 250$ counts at $t = 729 - 924$ ns). Time zero corresponds to the pixel with maximum intensity, $I(0)$; however, the first seven pixels after $t=0$ ns are excluded from fitting as they are convoluted with an instrumental artifact that extends over this region. The source of the artifact has been determined to be instrumentalⁱ, so does not have an effect on the solubilizate distribution nor kinetic model. The data is not deconvoluted with the instrument response function (IRF), because the small width relative to the time range has negligible convoluting effect.¹⁰ The LED pulse (<1.5 ns) and PMT detector response (180 ps) (specifications from Photon Technologies, Inc.) are short compared to the length of the experiment and, as such, the IRF occupies less than one channel ($2200\text{ns}/1024$ channels = 2.15 ns).

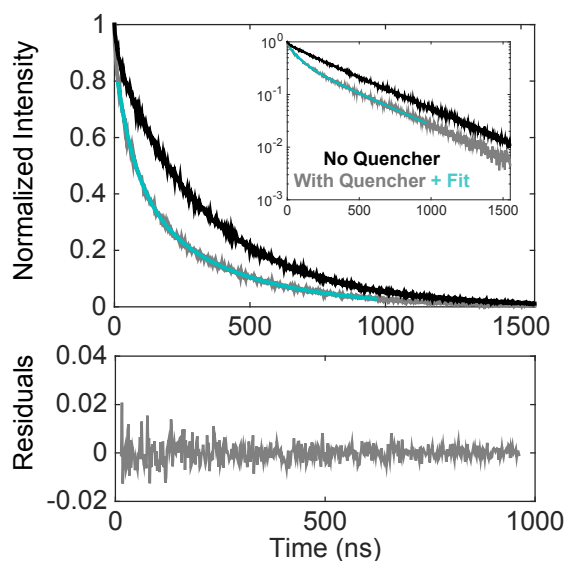


Figure S17. Representative TRFQ curves with and without quencher (normalized and background corrected) and residuals of the fit for decay curve with quencher.

Shape predictions from $\Delta N_{\text{agg}}/n_c$

The experimental values for $\Delta N_{\text{agg}}/n_c$ for the alkyl melibiosides is compared to the geometrically predicted values for various shapes and ellipticity as described by Tanford et al.²⁹ Tanford et al. have calculated the aggregation numbers for ellipsoids with varying ellipticity (semi-major axis/semi-minor axis ratio) and shape (prolate, oblate, spherical).

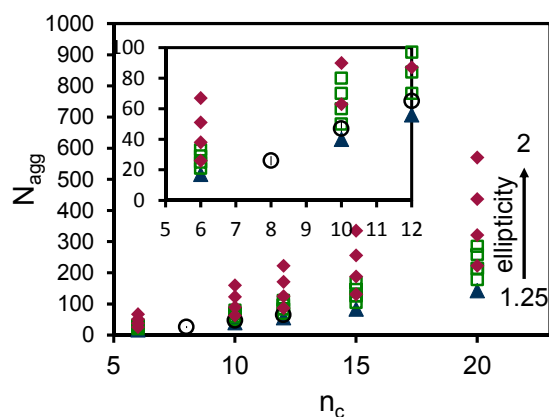


Figure S18. Aggregation number (N_{agg}) for varying number of carbons in alkyl chain (n_c) as determined experimentally for alkyl melibiosides (\bullet) and geometrically for oblate (\blacklozenge) or prolate ellipsoidal (\square) with ellipticities ranging from 1.25 to 2 and spherical (\blacktriangle) micelles. The inset shows a zoomed view of the region of interest.

Micropolarity index comparison

The micropolarity of the micelle was assessed using τ_0 , but can also be determined by the intensity ratio of the third to first vibronic peak in the pyrene steady-state fluorescence spectrum (I3:I1).^{25,30} The I3:I1 is 0.56 in water and 2.0 in hexane.³¹ Here, steady-state fluorescence measurements were acquired with the same instrumentation and conditions as the TCSPC measurements with additional parameters for steady-state measurements as follows: excitation at 337 nm with Xe-arc lamp (Photon Technologies, Inc.), emission spectral range of 350 - 550 nm, 0.25 nm step size, 0.05 s integration, and 0.5 nm slit width. τ_0 shows a trend with surfactant concentration, whereas the I3:I1 ratio does not (Figure S19.) The average %RSD for triplicate sample measurements of τ_0 and I3:I1 are 3.7% and 2.4%, respectively. τ_0 is more sensitive to polarity, and therefore was used throughout this work.

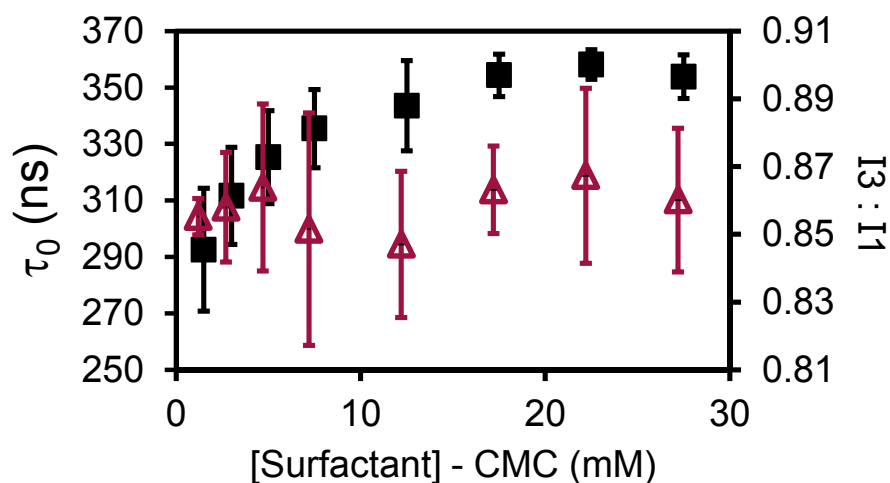


Figure S19. Comparison of micropolarity indices, fluorescence lifetime and I3:I1.

Dodecyl Cellobioside Phase Observations

Dodecyl cellobioside exhibits complex phase transitions at dilute concentrations. Solutions were sonicated for one hour, then left undisturbed. Partial gelation occurs on a short time scale. The gel phase transitions to a cloudy solution with time.

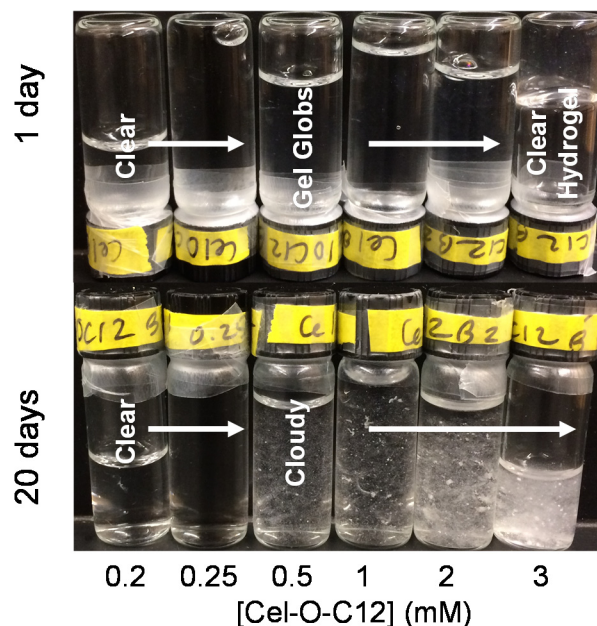


Figure S20. Photograph of dodecyl cellobioside solutions at various concentration and equilibration time. The upper series of vials is inverted to illustrate full gelation of the last vial, which remains in the bottom of the vial upon inversion.

REFERENCES

1. R. Pecora, *Dynamic Light Scattering*, Plenum Press, New York, 1985.
2. P. P. Infelta, M. Gratzel and J. K. Thomas, *J. Phys. Chem.*, 1974, **78**, 190-195.
3. P. P. Infelta and M. Gratzel, *Journal of Chemical Physics*, 1979, **70**, 179-186.
4. M. Maestri, P. P. Infelta and M. Gratzel, *Journal of Chemical Physics*, 1978, **69**, 1522-1526.
5. M. Tachiya, *J. Chem. Phys.*, 1982, **76**, 340-348.
6. P. P. Infelta, *Chemical Physics Letters*, 1979, **61**, 88-91.
7. G. G. Warr and F. Grieser, Determination of Micelle Size and Polydispersity by Fluorescence Quenching - Theory and Numerical Results, 82).
8. M. H. Gehlen and F. C. Deschryver, *Chemical Reviews*, 1993, **93**, 199-221.
9. R. Ranganathan, M. Peric and B. L. Bales, *Journal of Physical Chemistry B*, 1998, **102**, 8436-8439.
10. D. D. Miller and D. F. Evans, *J. Phys. Chem.*, 1989, **93**, 323-333.
11. M. Vanderauwaer, J. C. Dederen, E. Gelade and F. C. Deschryver, *Journal of Chemical Physics*, 1981, **74**, 1140-1147.
12. M. Gratzel, Kalyanasundaram, K., *Kinetics and Catalysis in Microheterogeneous Systems*, CRC Press, New York, 1991.
13. A. V. Barzykin and M. Tachiya, *Heterogeneous Chemistry Reviews*, 1996, **3**, 105-167.
14. M. W. Geiger and N. J. Turro, *Photochem. Photobiol.*, 1975, **22**, 273-276.
15. R. G. Alargova, Kochijashky, II, M. L. Sierra and R. Zana, *Langmuir*, 1998, **14**, 5412-5418.
16. M. Almgren and J. E. Lofroth, *J. Chem. Phys.*, 1982, **76**, 2734-2743.
17. A. Siemiarzuk, W. R. Ware and Y. S. Liu, *Journal of Physical Chemistry*, 1993, **97**, 8082-8091.
18. M. Vanderauwaer and F. C. Deschryver, *Chemical Physics*, 1987, **111**, 105-112.
19. LogKow, a databank of evaluated octanol-water partition coefficient, ICSU-CODATA., <http://logkow.cisti.nrc.ca/logkow/>, (accessed 2014, 2014).
20. Z. Wenjun and Z. Lizhong, *Colloids and Surfaces A (Physicochemical and Engineering Aspects)*, 2005, **255**, 145-152.
21. A. V. Barzykin, *Chemical Physics Letters*, 1992, **189**, 321-327.

22. M. Almgren, J. Vanstam, S. Swarup and J. E. Lofroth, *Langmuir*, 1986, **2**, 432-438.
23. R. Zana, M. Benraou and B. L. Bales, *J. Phys. Chem. B*, 2004, **108**, 18195-18203.
24. P. Somasundaran, *Encyclopedia of Surface and Colloid Science*, CRC Press, Taylor & Francis Group, Boca Raton, FL, 2006.
25. K. Kalyanasundaram and J. K. Thomas, *J. Am. Chem. Soc.*, 1977, **99**, 2039-2044.
26. H. R. Li, F. Gao, C. H. Tung and L. Z. Wu, *Chinese Journal of Chemistry*, 2000, **18**, 506-509.
27. J. B. Birks, I. H. Munro and D. J. Dyson, *Proceedings of the Royal Society of London Series a-Mathematical and Physical Sciences*, 1963, **275**, 575-+.
28. J. Aguiar, P. Carpena, J. A. Molina-Bolivar and C. C. Ruiz, *Journal of Colloid and Interface Science*, 2003, **258**, 116-122.
29. C. Tanford, *J. Phys. Chem.*, 1972, **76**, 3020-3024.
30. D. S. Karpovich and G. J. Blanchard, *Journal of Physical Chemistry*, 1995, **99**, 3951-3958.
31. A. Malliaris, *International Reviews in Physical Chemistry*, 1988, **7**, 95-121.

The artifact persists regardless of fluorophore type (anthracene or pyrene) and concentration, solvent environment (cyclohexane, water, ethanol, and various surfactant systems), slit width, excitation source, further deoxygenation (multiple freeze-pump-thaw processes and Ar-purging), and cuvette (and silanization). It cannot be attributed to excimer formation (below necessary concentration and no excimer fluorescence observed in steady-state emission spectrum at excimer emission wavelength of 490 nm) nor solubilization in multiple environments (2nd lifetime is << 45 ns).